Please cite this paper as: Amorosi A., Rollo F., Di Santo G. (2023). A micro-inspired perspective on the constitutive modelling of clays. *Rivista Italiana di Geotecnica*, 4, 3-22. dx.doi.org/10.19199/2023.4.0557-1405.003.

# A micro-inspired perspective on the constitutive modelling of clays

Angelo Amorosi,* Fabio Rollo,* Giacomo Di Santo*

*Summary*

Clays are ubiquitous in geotechnical and environmental engineering applications and understanding their complex mechanical behaviour is essential for designing and constructing safe and efficient structures. Over the years, numerous constitutive models have been developed to describe their mechanical behaviour, but only few of them were formulated explicitly accounting for the complex microstructural behaviour of these materials.

The aim of this paper is providing an overview of some recent advances in micro-inspired constitutive modelling of clays. After a review of multi-scale experimental evidence and its possible interpretation and generalisation in terms of internal variables controlling the mechanics of clayey soils, two examples of constitutive models are proposed, both developed in the framework of Thermodynamics with Internal Variables. This theoretical environment proves to effectively allow the development of constitutive models that not only respect the fundamental principles of thermodynamics, but also directly benefit from our understanding of the complex micromechanics of clayey soils.

Keywords: porosity, fabric, clay, constitutive modelling, thermodynamics.

## 1. Introduction

Soil mechanics is a well-established discipline that has always put considerable emphasis on the physical characteristics of the studied materials, whose peculiarity lies in their granular and multi-phase nature.

In fact, each series of introductory lectures at University level qualitatively emphasises the substantial role played by individual particles and, when present, their aggregates on the behaviour of the overall soil skeleton, highlighting the intricacy of the multi-physical interactions occurring at the micro-scale. The complexity increases as the particle size decreases, reaching the highest complexity in clayey soils.

Unfortunately, this premise often leads to a potential disappointment of the same class of students when they are first introduced to the mechanical behaviour of soils in general, and of clays in particular, at the continuum level, as most of the microstructural features previously discussed are only marginally considered in such a quantitative context, erroneously implying that the micro and macro scales are broadly independent. This is obviously not true, as shown by the huge amount of research carried out in this field. In fact, several research attempts aimed at linking microscopic features to macroscopic patterns of behaviour have characterised the whole history of soil mechanics (*e.g.*: Terzaghi, 1948; Mitchell, 1956; Smart, 1969; Smart and Tovey, 1982), proposing either qualitative or, more recently, quantitative means to bridge the gap between scales.

This paper firstly aims to summarise some experimental evidence on the role of the microstructural characteristics of clayey soils on their mechanical behaviour, in order to provide a guide to the selection of relevant internal variables, *i.e.* state variables that condense microscopic mean characteristics and make them suitable to be incorporated into a macroscopic constitutive modelling framework. In light of the above, the specific modelling approach based on Thermodynamics with Internal Variables (TIV) (*e.g.*: Maugin and Muschik, 1994) is then outlined and specialised to the case of clays, illustrating some recently obtained results.

In the following, the soil mechanics sign convention (compressive positive) is assumed, and all stresses are effective stresses. Second order tensors are mainly expressed by boldface notation, with subscript notation only used when necessary, *e.g.* summation is denoted by repeated indexes.

## 2. Experimental evidence

Two fundamental clays microstructure descriptors are here considered: porosity and fabric.

As will be shown in the following, they are natural candidates to play the role of internal variables, given their substantial influence on the macroscop-

* Sapienza Università di Roma, Department of Structural and Geotechnical Engineering, Italy

ic mechanics of clays, their evolving character, and their property of being in principle measurable but not controllable at each stage of their evolution.

Porosity and fabric share some common features. One is the scale dependency, which leads to different pictures depending on the scale adopted in the observation. Another one consists in the current strong technological constraints that limit direct experimental observations at the microscale only to *post-mortem* conditions, *i.e.* at the end of any test, thus limiting our capability to follow their evolution *in-situ*, which, in the jargon adopted by the multi-scale experimental community, means "during the test".

### *2.1. Porosity*

The classical definition of porosity $n$ adopted in soil mechanics refers to the ratio of the volume of voids to the total volume of the macroscopic soil element. Equivalent scalars are alternatively adopted to express related measures, as the specific volume $v$ or the void ratio $e$. The above mean variables can be evaluated by standard mass-volume relationships.

The careful observation of thin sections of a clayey sample by scanning electron micrography (SEM) reveals a more complex picture of the microstructure and its articulate patterns in terms of porosity: in fact, as originally proposed by OLSEN [1962] and BARDEN and SIDES [1970] and then confirmed by many others (*e.g.* DELAGE and LEFEBVRE, 1984; HICHER *et al.,* 2000; HATTAB *et al.,* 2013), the material can be schematised as composed by an aggregated microstructure in which larger pores characterise the inter-aggregate volumes while smaller ones are observed within the aggregate (intra-aggregate pores). The dual regime of porosity is schematically represented in figure 1 with reference to a kaolinite clay [YU *et al.,* 2016] and supported by SEM images.

This is also confirmed by mercury intrusion porosimetry (MIP) data, often showing bimodal patterns in the pore size distribution curves, especially with reference to soft natural or reconstituted clays. Although both SEM and MIP techniques are subjected to continuous improvements in terms of accuracy and reliability, comparing measurements of pore size distributions obtained by them does not always lead to the same outcome, as discussed in ZHENG *et al.* [2022].

In spite of these limitations, it is possible to trace the mechanically induced evolution of porosity at different scales by interrupting any geotechnical test, cutting the sample in a representative number of portions and, after drying, subjecting them to SEM and MIP measurements. This procedure has been applied to both reconstituted and intact clays, characterised by different mineralogy, while being subjected to either proportional stress paths, as the isotropic or oedometric ones, or to deviatoric tests (*e.g.* HICHER *et al.,* 2000; HATTAB and FLEUREAU, 2010; MITARITONNA et *al.,* 2014; YU *et al.,* 2016; CHOW *et al.,* 2019; GAO *et al.,* 2020; GUGLIELMI et al., 2022; ZHENG *et al.,* 2022).

The above observations can be used to sketch a simplified interpretation of the microscopic response of a sample of reconstituted clay subjected to virgin radial compression, just after its transition from slurry to solid state, up to soft to medium consistency states: it mainly experiences a volume reduction of the inter-aggregate pores, which corresponds to the macroscopic evolution of the mean porosity as expressed by $n$ or $v$, while intra-aggregate pores remain almost unchanged (*e.g.* GUGLIELMI *et al.,* 2022; ZHENG *et al.,* 2022). This is clearly shown in figure 2 with reference to MIP measurements performed by YU *et al.* [2016] on a kaolinite clay. A modification of the inter-aggregate pores size distribution is observed when the clay is subjected to isotropic consolidation at mean effective pressure of 100 kPa and

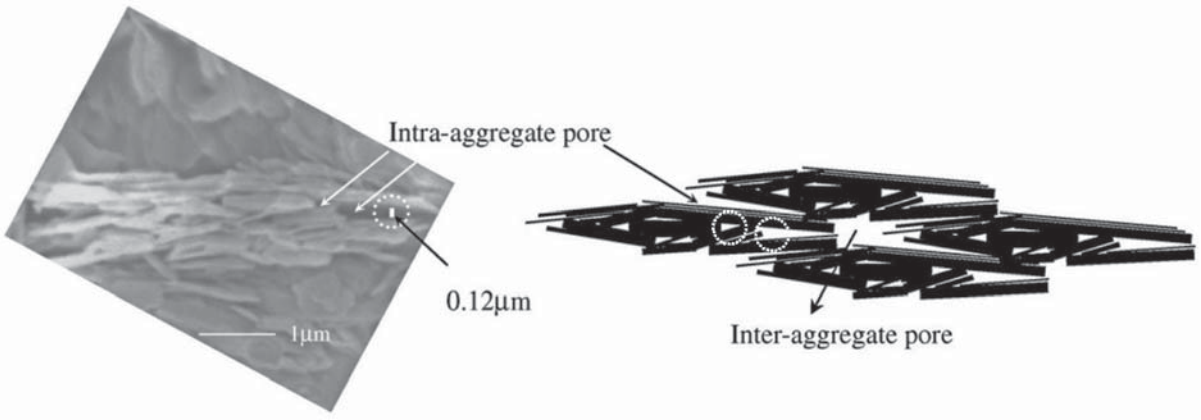


Fig. 1 – Illustration of the double porosity: intra-aggregate pores and inter-aggregate pores for edge-to-face contact (modified from YU *et al.*, 2016).

*Fig. 1 – Spiegazione della doppia porosità: vuoti intra-aggregato e inter-aggregato per contatti edge-to-face (modificata da Yu* et al.*, 2016).*

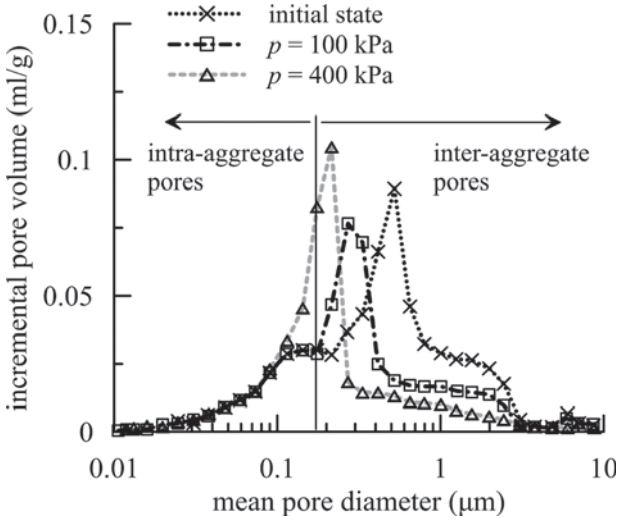


Fig. 2 – Results of MIP analyses in terms of incremental pore volume vs mean pore diameter after slurry consolidation and after different isotropic stress states (modified from Yu *et al.*, 2016).
*Fig. 2 – Risultati delle analisi MIP in termini di volume incrementale dei vuoti rispetto al diametro medio dei vuoti dopo la consolidazione dello slurry e dopo diversi stati tensionali isotropi (modificata da Yu* et al.*, 2016).*

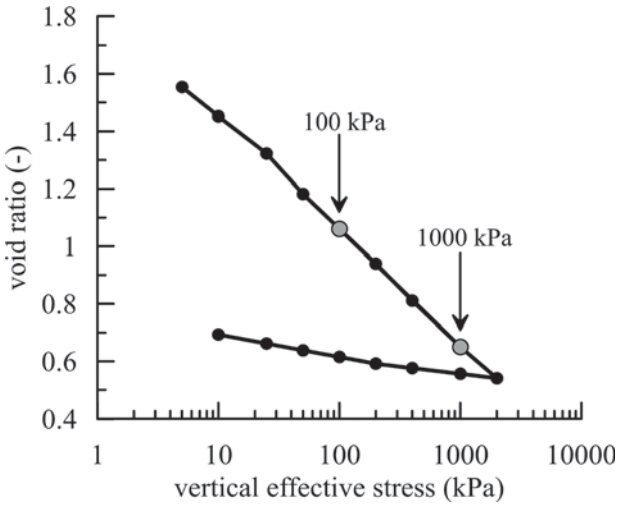


Fig. 3 – Oedometric compression and swelling curves for a reconstituted illitic clay (modified from Zheng *et al.*, 2022).
*Fig. 3 – Curve di compressione edometrica e curve di rigonfiamento per un'illite ricostituita (modificata da Zheng* et al.*, 2022).*

400 kPa after the initial consolidation in the slurry, while the intra-aggregate volumes remain stable.

A similar trend is observed by Zheng *et al.* [2022] on a reconstituted illitic clay subjected to oedometric compression as shown in figure 3. In fact, analogously to Yu *et al.* [2016], MIP measurements reveal a modification of the inter-aggregate pores distribution during the loading process, also confirmed by SEM images taken for the specimens for vertical effective stresses of 100 kPa and 1000 kPa shown in figure 4. In detail, techniques of digital image processing of the SEM pictures (Fig. 4b,d) allow to map the distribution and the morphology of the inter-aggregate pores and to detect the reduction of the voids volume and the modification of their aspect ratio during compression.

Similarly, during triaxial compression drained tests, the shearing process alters the size of the inter-aggregate pores, leaving the intra-aggregate ones almost unchanged [Yu *et al.*, 2016]. This pattern supports the findings numerically obtained by Anandarajah [2000a, b], indicating that, at least for the idealised clays investigated by the Author, the mechanical behaviour depends on the aggregate-to-aggregate interactions, rather than on the particle-to-particle pores. Some Authors also infer that, especially in non-active clays, the aggregate-to-aggregate interaction is mainly characterised by frictional contacts in which the surface-related electro-chemical forces are negligible [Chang *et al.*, 2009; Yu *et al.*, 2016], while others [Hattab and Chang, 2015; Pedrotti and Tarantino, 2018] provide a more elaborate picture in which non-contact forces play a role in the mechanical behaviour of the investigated clayey soil.

It should be remarked that the general interpretation in terms of double porosity provided above holds until a relatively high level of stress is attained: at that stage inter-aggregate pores exhibit a size comparable to that of the intra-aggregate ones, leading to a unimodal pore size distribution, whose mean value turns out to be the one controlling the behaviour of the soil [Guglielmi *et al.*, 2022].

The microstructural insight summarised above appears to be consistent with the well-established Critical State Soil Mechanics framework (CSSM), which first considered the fundamental role of the porosity, via $v$, on each aspect of the mechanical behaviour of clays, thus extending the set of state variables that up to that moment had been limited to the sole effective stress state. In this framework the irreversible variation of the void ratio, as read on the virgin compression line, controls the evolution of the mechanics of the material leading, in an elasto-plastic setting, to the isotropic volumetric hardening law of the Cam-Clay family constitutive models.

### *2.2. Fabric*

In granular mechanics, the term fabric refers to the orientation-related characteristics of the material at the grain scale. In clays, given their aggregated microstructure, it is possible to define different fabrics with reference to different scales: for observations carried out at the scale of about 1 μm, *i.e.*

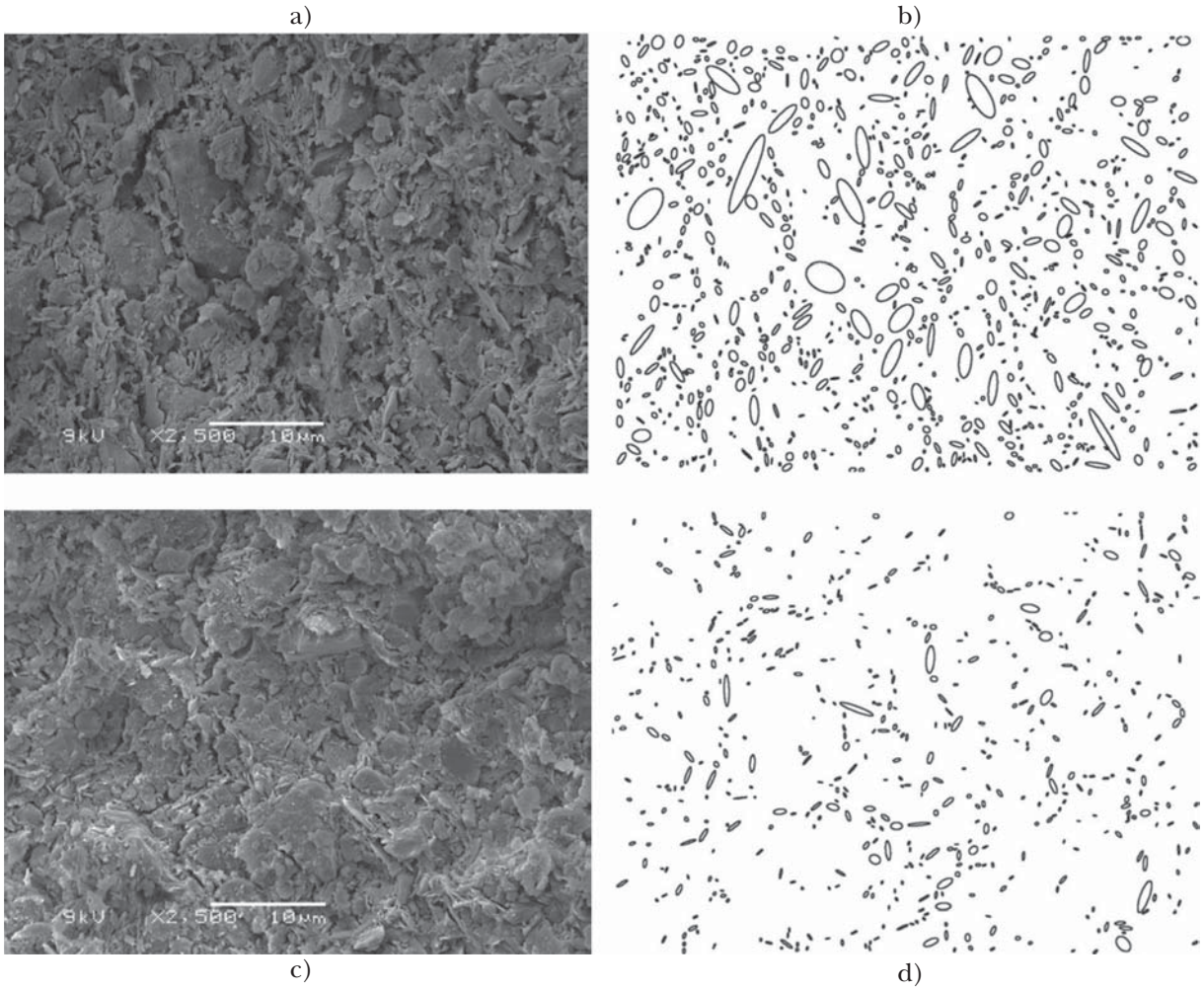


Fig. 4 – SEM images of the vertical plane of the reconstituted clay and pores distribution obtained through SEM pictures processing for the 1D consolidation pressure of 100 kPa a), b) and 1000 kPa c), d) (modified from ZHENG *et al.*, 2022).
*Fig. 4 – Immagini SEM di una sezione verticale dell'argilla ricostituita e della distribuzione dei pori ottenuta attraverso l'elaborazione di immagini SEM per la pressione di consolidazione 1D di 100 kPa a), b) e 1000 kPa c), d) (modificata da* ZHENG et al., *2022).*

roughly corresponding to the single particle dimension, the fabric will be representative of the intra-aggregate, while the orientation pattern emerging at the scale of tens of microns should be interpreted as that of the aggregates.

In mechanics the quantitative description of fabric is condensed in a tensorial entity named fabric tensor [KANATANI, 1984; FU and DAFALIAS, 2015] which, in the following, will be restricted to second order. In its original formulation, the fabric tensor is defined as:

$$\mathbf{F} = \frac{1}{N}\sum_{k=1}^{N} \mathbf{n}^k \otimes \mathbf{n}^k \qquad (1)$$

where $N$ is the number of the particles/aggregates being quantified in the domain, $\mathbf{n}$ is the direction-related unit vector, $\otimes$ is the tensor product and the superscript $k$ refers to the $k$th grain/aggregate. In principle, once the scale of observation is set, it is possible to identify the direction $\mathbf{n}^k$ of each particle/aggregate in the reference volume so to define the overall directional probability density function and calculate, by equation (1), the corresponding fabric tensor $\mathbf{F}$, which is characterised by a normalised trace. Assuming the observation is carried out in 2D, as costumary for SEM-based images, the second order fabric tensor reduces its degrees of freedom to two, *i.e.* it can be fully described by two scalar values: 1) the major principal direction (typically expressed by an angle with respect to a fixed reference in the plane of analysis), which represents the predominant orientation of the $N$ particles/aggregates and 2) a relation between its two principal components $F_1$ and $F_2$, such as $F_1/F_2$ or $F_1$-$F_2$, related to the degree of anisotropy or, in other terms, to the scatter of the directional distribution with respect to its major principal direction defined in 1).

Alternative but equivalent definitions have been proposed in the past and are often adopted in the interpretation of SEM images: among them, it is worth recalling here that outlined in the approach proposed by MARTINEZ-NISTAL *et al.* [1999]. It requires a digital processing of the SEM image at the relevant scale, by the analysis of the brightness intensity of the

pixels. At this stage, elongated bright regions in the image are interactively thinned to line-shaped regions. These are processed through filtering to derive, based on a brightness threshold, a binary image in which lines complying with the threshold are considered of interest. These are thinned to a pixel width and the fabric orientation is calculated from the texture line map using a line-following algorithm to obtain polygonal lines, whose segments are logged in terms of length and orientation (vectors). A rose histogram is then used to represent the vector lengths $l_i$, for each direction range, $\theta_i$ (interval 10°). A statistical analysis of the vector lengths results in both the mean direction of all the vectors $\theta$, and a scalar statistical expression of the dispersion of the vectors with respect to the mean direction $\overline{L}$:

$$\theta = \tan^{-1}\left[\frac{\sum_{i=1}^{n} l_i \sin\theta_i}{\sum_{i=1}^{n} l_i \cos\theta_i}\right] \quad (2)$$

$$L = \sqrt{\left(\sum_{i=1}^{n} l_i \cos\theta_i\right)^2 + \left(\sum_{i=1}^{n} l_i \sin\theta_i\right)^2} \quad (3)$$

$$\overline{L} = \frac{L}{\sum_{i=1}^{n} l_i} \quad (4)$$

Given the expression of $\overline{L}$, its values characterising different degrees of orientation are not of uniform size:

$\overline{L}$ =1: maximum degree of iso-orientation;

$0.21 < \overline{L} < 1$: very oriented fabric;

$0.15 < \overline{L} < 0.21$: low oriented fabric;

$\overline{L} < 0.15$: random oriented fabric.

Quantitative evaluation of the directional patterns at the microscale and their evolution during proportional stress path and/or shearing have been presented, among others, by Cotecchia and Chandler [1998]; Hicher *et al.* [2000]; Cetin [2004]; Hattab and Floreau [2010]; Mitaritonna *et al.* [2014]. All the above studies indicate that the previously experienced virgin compression, if sufficiently extended, leads to a consistently oriented microstructure. This is, for example, the case of reconstituted clayey samples initially compressed in a consolidometer from their slurry state, leading to an orientation pattern at the microscale that is consistent with the applied 1D compression conditions. If the same material is then subjected to a sufficiently extended isotropic compression, it smoothly modifies the orientation of its components towards a more dispersed (*i.e.* less oriented) conditions. The picture becomes less clear when applying deviatoric paths up to failure: in fact, strain localisation often occurs, implying the coexistence, within the same specimen, of rather different orientation patterns at the microlevel. Figure 5 shows a schematic representation of the fabric for different states of an oedometric compression as proposed by Chow *et al.* [2019]: this picture suggests that fabric can be quantified through either aggregates or voids orientation and can evolve during the loading process.

Just like what discussed for porosity, the above references confirm that the quantitative description of fabric at the scale of about 1 μm, *i.e.* roughly corresponding to the single particle dimension, provides a picture that can be rather different, and often less significative, from that emerging with respect to the

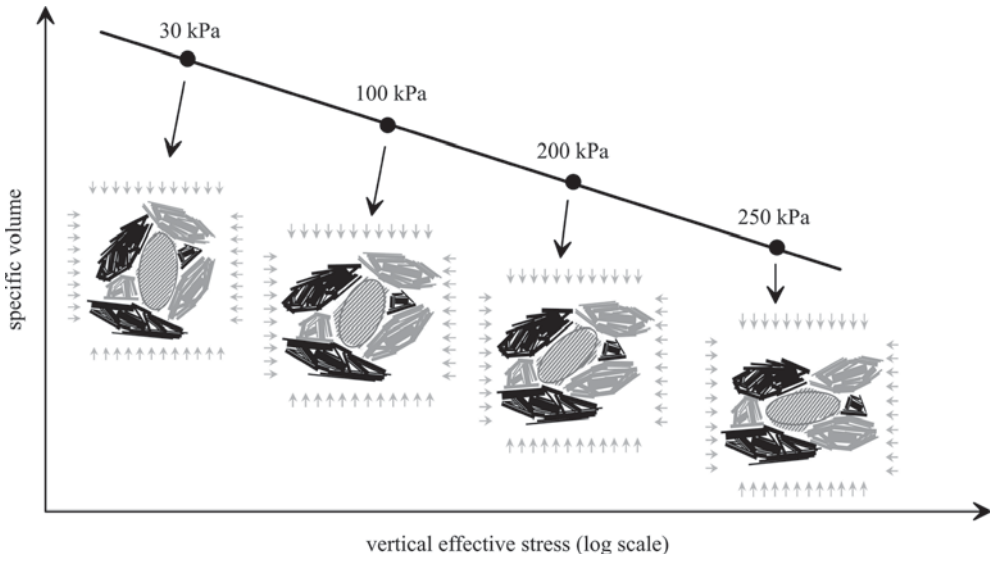


Fig. 5 – Schematic representation of the fabric evolution during oedometric compression. The pictures show the modification of the aggregates and voids orientation during the loading process (modified from Chow *et al.*, 2019).

*Fig. 5 – Schema dell'evoluzione del fabric durante una compressione edometrica. Le immagini mostrano la modifica dell'orientamento degli aggregati e dei vuoti durante il processo di carico (modificata da* Chow et al.*, 2019).*

scale of tens of microns, *i.e.* that of the aggregates, at least for relatively soft natural and reconstituted clays. In fact, the careful observation of fabric during virgin radial stress paths highlights that the key processes are occurring at this latter scale, where the aggregates exhibit a well-defined directional evolution, not necessarily accompanied by a comparably evident evolution of the intra-aggregate particle orientations (*e.g.* MITARITONNA *et al.,* 2014). This picture is consistent with that provided by ANANDARAJAH [2000a, b] in his pioneering attempt to model the behaviour of clays by a DEM approach.

The macroscopic effect of the orientational patterns discussed above is anisotropy. This crucial aspect of the mechanical behaviour of soils, in general, and clays in particular, affects the full range of their mechanical behaviour, including the reversible elastic behaviour, as detected by very small stress–strain perturbations (*e.g.* PENNINGTON *et al.,* 1997; ZDRAVKOVIC and JARDINE, 1997) and the irreversible plastic response, as for the orientation of the yield domain in the stress space resulting from careful probing from the *in situ* state [SMITH *et al.,* 1992; CALLISTO and CALABRESI, 1998; KIM and FINNO, 2012], up to the response at critical state, as discussed in LI and DAFALIAS [2012].

Both elastic and plastic anisotropy of clayey soil display an evolving character when the material is subjected to sufficiently extended radial stress paths (*e.g.* GENS, 1982; MITARITONNA *et al.,* 2014). In fact, they seem to evolve in a consistent way, being the plausible macroscopic manifestation of clay's internal evolving microstructure. This common physical basis supports the idea of introducing a unique tensorial variable in the constitutive modelling of clays at the macroscopic level, capable of accounting for all the above discussed directional properties as suggested in AMOROSI *et al.* [2021] within the framework of elasto-plasticity, along the line of the pioneering work of HUECKEL and TUTUMLUER [1994]. Essentially, it was proposed to combine anisotropic hardening laws, describing the evolution of a fabric tensor-related variable controlling the distortion of the yield domain in the stress space (*e.g.* KAVVADAS, 1982; DAFALIAS, 1986) with corresponding elastic formulations also dependent on a second order tensor related to the fabric one. This perspective is further developed in a different theoretical framework in the final part of this contribution.

## 3. Wave propagation as a proxy for clay microstructure

This section presents a brief literature review on the use of measurement of shear wave velocity in laboratory experiments and field measurements to obtain information on soil porosity and fabric. The objective is to demonstrate the link between these two different aspects, highlighting the great potential of wave propagation technique of indirectly acquiring average information on porosity and fabric, thus allowing to carry out *in situ* observations, *i.e.* during a test, rather than limiting the microstructural data acquisition to the *post-mortem* stages.

### *3.1. Laboratory investigations*

In this paragraph the key results emerging from MITARITONNA *et al.* [2014] are summarised, aiming at providing a picture of the evolving microstructural features of a reconstituted clay, as observed during laboratory experiments, and their relation with the evolving reversible response, as detected propagating shear waves polarised along different planes.

MITARITONNA *et al.* [2014] present the results from a series of tests carried out on reconstituted Lucera clay, a mainly illitic medium plasticity clay of marine origin. Triaxial tests were performed by stress-controlled systems fitted with horizontal multi-directional bender elements to determine the dynamic shear moduli $G_{ij}$, where the subscripts $i$ and $j$ denote the direction of wave propagation and polarisation, respectively. The testing programme was designed to investigate the evolution of clay stiffness in general and stiffness anisotropy in particular, this latter described by the ratio $G_{hh}/G_{hv}$, along constant stress ratio $\eta$ virgin compression paths attaining mean effective stresses ($p=1/3\mathrm{tr}(\boldsymbol{\sigma})=1/3\sigma_{ii}$) much higher (up to $p \approx 1350$ kPa) than those previously imposed in a consolidometer ($p \leq 70$ kPa) and, at some stages, also imposing unloading-reloading branches. The values of $\eta$ applied in the different tests ranged from 0 to 0.8, as illustrated in figure 6. Only two tests (4 and 5) were characterised by a variation of the consolidation stress ratio, while all the others were carried out at constant $\eta$. Thin vertical sections of the specimens were prepared, either at the end of the consolidometer stage or of the triaxial radial compression paths, to be then analysed by SEM at the scale of the tens of microns, *i.e.* corresponding to the aggregates one, quantitatively elaborating the images by the approach proposed by MARTINEZ-NISTAL *et al.* [1999].

The observed values of $G_{hh}/G_{hv}$ at the equilibrium states during the stress paths tests are plotted versus $p$ in figure 7, where the stiffness ratios, measured at normally consolidated equilibrium states along the different constant-η compression paths, are joined with different curves.

For $p$ values below the consolidometer-preconsolidation pressure, *i.e.* for initially overconsolidated states, all the different test data are located on about a single horizontal line, corresponding to $G_{hh}/G_{hv} \approx$ 1.12-1.13; this observation suggests that up to this stress level the shear stiffness ratio is not significantly influenced by the differences in stress ratio $\eta$ applied

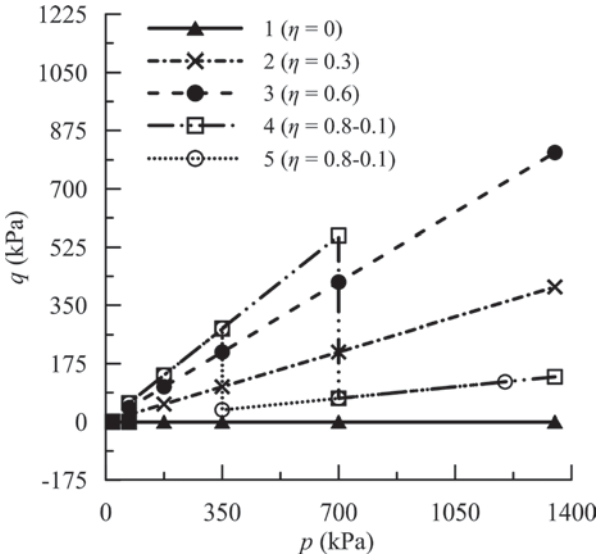


Fig. 6 – Testing programme (modified from Mitaritonna *et al.*, 2014).
*Fig. 6 – Programma di prova (modificata da Mitaritonna* et al.*, 2014).*

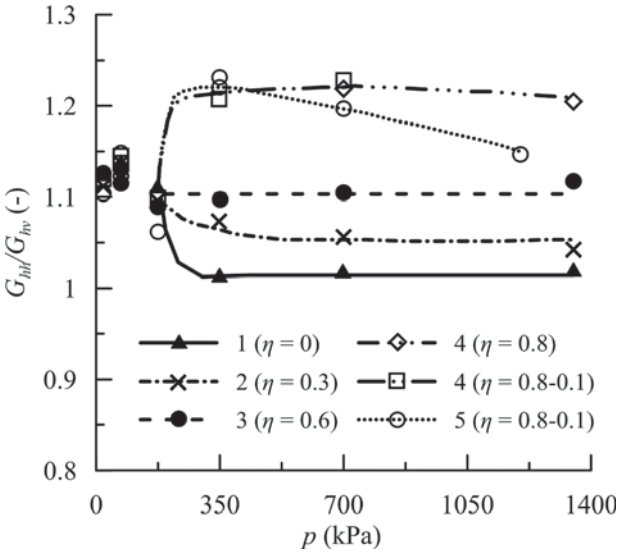


Fig. 7 – Shear stiffness anisotropy evolution (modified from Mitaritonna *et al.*, 2014).
*Fig. 7 – Evoluzione dell'anisotropia elastica (modificata da Mitaritonna* et al.*, 2014).*

in the recompression of the clay. Therefore, in its initial overconsolidated state, the clay is characterised by a stiffness anisotropy ratio $G_{hh}/G_{hv} \approx 1.12$. This value is related to the directional character developed by the clay microstructure during one-dimensional consolidation from slurry in the consolidometer: in fact, the analysis of the corresponding SEM pictures indicates an average direction $\theta = 32°$ with respect to the horizontal and a degree of anisotropy $\overline{L} = 0.28$, corresponding to a very oriented fabric (Fig. 10a).

When further radially compressed beyond its initial yield stress, the stiffness ratio either decreases, as in tests 1 and 2, or increases, as in tests 4 and 5, prior to reaching a constant value, at about $p \approx 350$ kPa, which depends on the imposed stress ratio $\eta$.

During test 3, corresponding to $\eta = 0.6$, the anisotropy ratio is always about $G_{hh}/G_{hv} \approx 1.11$, a value close to the post-consolidometer one. This is consistent with the hypothesis that the stress ratio the soil was subjected to in the 1D compression in the consolidometer was equal to that applied in test 3, $\eta = 0.6$, due to a $K_0 = 0.56$, as predicted by Jaky [1944], for the clay under study. In fact, at the end of test 3 the SEM image, shown in figure (5), indicates a degree of anisotropy, $\overline{L} = 0.27$, very similar to the initial one and a lower mean direction $\theta = 7°$, which highlights the further microstructural reorientation experienced by the material along the persistent $K_0$ conditions imposed in the triaxial system. A careful inspection of the SEM images indicates that during test 3 the most relevant microstructural modification consists in the reduction of the inter-aggregate pores in the virgin compression stages, on average characterised by an initial equivalent diameter of about 10 μm, then reducing to 5 μm at the end of the test. This is confirmed by the conventionally evaluated specific volume $v$, which varies along the virgin compression line (Fig. 8): as expected, upon the unloading-reloading stages, $v$ experiences minor changes, fully recovered when back on the virgin compression line. Figure 9 shows the evolution of $G_{hv}$ and $G_{hh}$ against $p$ in a bi-log plot, clearly highlighting the well-known dependence of the elastic stiffness moduli on the current effective stress state and on the previously experienced virgin stress-strain history. In fact, along each unloading-reloading branch, *i.e.* for each attained value of the preconsolidation pressure $p_c$ and/or the corresponding specific volume $v$ read on the virgin compression line, the moduli vary non-linearly with $p$; when subjected to further compression along the virgin compression line, thus inducing permanent variation of the specific volume, the clay experiences an irreversible modification of its microstructure in terms of porosity which affects the subsequent stiffness measurements, leading to augmented $G_{hv}$ and $G_{hh}$ values, as observed along the following unloading-reloading branches.

Compression paths characterised by stress ratio $\eta = 0$ (test 1) and 0.3 (test 2), lower than the initial $\eta = 0.6$, induce a permanent reduction in the degree of anisotropy, leading to $G_{hh}/G_{hv} \approx 1.05$ for $\eta = 0.3$ and about 1.01 for $\eta = 0$. This is confirmed by the analysis of the SEM image shown in figure 10b, obtained at the end of test 2, characterized by a mean direction $\theta = 5°$ and $\overline{L} = 0.13$, typical of a randomly oriented fabric.

On the contrary, the anisotropy ratio increases up to 1.22 during test 4, where the soil was mostly

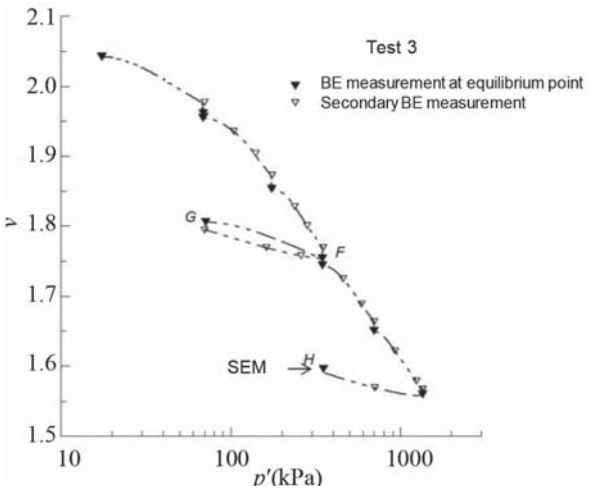


Fig. 8 – Test 3: compressibility plot and BE measurements (modified from MITARITONNA *et al.*, 2014).
*Fig. 8 – Test 3: piano di compressibilità e misure con BE (modificata da* MITARITONNA et al.*, 2014).*

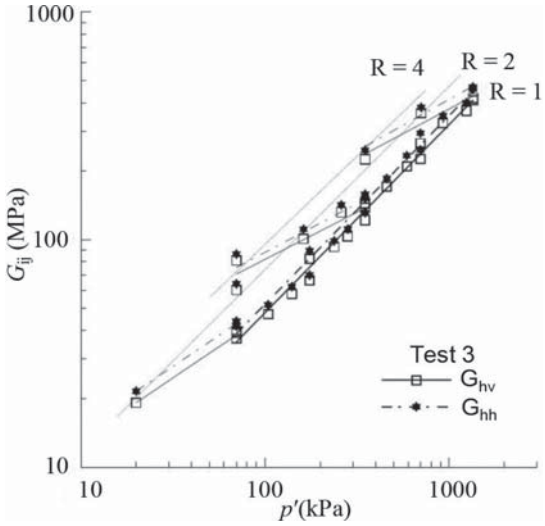


Fig. 9 – Evolution of $G_{hh}$ and $G_{hv}$ during Test 3.
*Fig. 9 – Evoluzione di $G_{hh}$ e $G_{hv}$ durante il Test 3.*

compressed along the highest ratio $\eta = 0.8$. Even this evidence finds its microstructural confirmation in the results of the analysis of the SEM image shown in figure 10, referred to the end of test 4, where $\theta = 2°$ and $\overline{L} = 0.37$, corresponding to a very oriented fabric. It is worth noting that in test 4 the stress ratio $\eta$ has been decreased from 0.8 to 0.1 at $p = 700$ kPa and then compressed at constant $\eta = 0.1$ up to $p = 1350$ kPa. Figure 7 shows that the anisotropy ratio reduces only slightly (from 1.22 to 1.21) along the new $\eta$ path. This observation suggests that the anisotropy induced in the material by constant-$\eta$ compression up to relatively high pressures ($p = 700$ kPa in this case) can be modified by further compression under different $\eta$ values only when reaching effective stress levels larger than twice those previously applied along the initial $\eta$-constant path. To corroborate this evaluation, a similar test was carried out, during which the stress ratio was reduced from 0.8 to 0.1 at $p = 350$ kPa and then compression at $\eta = 0.1$ was further developed, up to $p = 1350$ kPa (Test 5). In this case, a progressive reduction of the shear stiffness ratio, down to a value of 1.15 is recorded. The results of tests 4 and 5 lead to the conclusion that a change in degree of shear stiffness anisotropy is possible when $\eta$ varies, although it requires large plastic straining, as a small amount of irreversible deformation under the new $\eta$ is not sufficient to significantly modify the previously acquired directional character of the soil. This conclusion is consistent with what suggested by LEWIN [1973] in his pioneering work on the evolving character of the plastic potential of clays: a different, though related, aspect of the mechanics of clay.

In brief, for an approximately constant fabric configuration of the clay, as in test 3, the reversible response of the reconstituted Lucera clay varies - non linearly - with the effective stress state and the specific volume read on the virgin compression line at the preconsolidation pressure, this latter reflecting the microstructural configuration of the material in terms of porosity. Permanent changes in porosity, induced by further compression of the specimen along the virgin compression line, are mirrored in a scaling factor that equally affects both stiffness moduli $G_{hv}$ and $G_{hh}$. On the other hand, if the clay experiences differently oriented virgin radial stress-strain paths, sufficiently extended to induce a microstructural modification in terms of fabric, this reflects into a modification of the stiffness anisotropy making the reversible behaviour of the soil not only dependent on the current effective stress state and (virgin compression-related) porosity but also on the fabric tensor which accounts for the mean microscopic directional properties of the clay at the macroscopic level.

In conclusion, the above evidence clearly shows the intimate relationship between the micro-features of a reconstituted clay in terms of porosity and fabric and its reversible macroscopic response, observed through the propagation of polarised waves along different planes, providing a means to gain indirect insight into the microscopic patterns of the material while conducting laboratory tests, *i.e.* while exploring its macroscopic behaviour at different states.

### *3.2. Field investigations*

The field measurement of the shear waves velocity propagated through seismic down-hole and cross-hole tests is commonly used to evaluate the profile of the elastic shear moduli with depth. However, the same techniques allows to acquire useful information

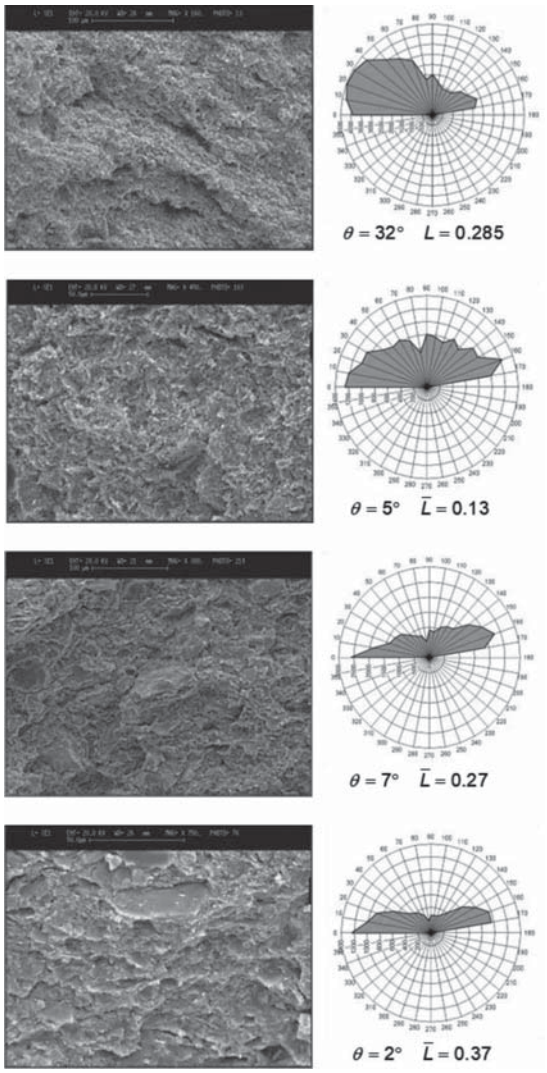


Fig. 10 – SEM segmented pictures and directional histograms. Top to bottom, after: consolidometer stage, Test 2, Test 3 and Test 4.

*Fig. 10 – Segmentazione tramite immagini SEM e diagrammi a rosetta. Dall'alto in basso: dopo fase in consolidometro, Test 2, Test 3 e Test 4.*

on the soil porosity (*e.g.* Foti *et al.*, 2002; Foti and Lancellotta, 2004; Uyanik, 2019). Foti *et al.* [2002] developed a rigorous procedure based on the theory of linear poroelasticity [Coussy, 2004] in the range of low frequencies for determining porosity in saturated soils as an explicit function of the compressional (P) and shear (S) wave velocities, the grain and fluid densities, the Poisson ratio of the solid skeleton and the bulk modulus of the solid particles. The results presented by Foti *et al.* [2002] match very well with a series of independent experimental observations obtained from standard laboratory tests on undisturbed samples and demonstrate that this approach is more reliable and theoretically sound than earlier empirical relationships that are often affected by uncertainties related to the soil type, mineralogy and the stress history. Moreover, the use of non-destructive and high quality seismic measurements (*e.g.* cross-hole test) allows to collect a greater amount of data as compared to those commonly determined on a limited number of samples in the laboratory, and to deduce the profiles of porosity with depth according to the natural state of the deposit while avoiding the effects of sampling disturbance.

Along the same track, additional studies have been extended to unsaturated soils. In this case, the three-phasic nature of the soil does not allow to fully characterise the porosity distribution with seismic tests only: this is why geo-electric and geo-seismic measurements can be coupled to improve the interpretation and the reliability of the results, as for measurement of electrical resistivity through field velocity resistivity probe (FVRP) (*e.g.* Yoon and Lee, 2010; Cosentini and Foti, 2014).

In field testing, the down-hole tests produce a horizontally polarised vertically travelling shear wave $V_{S,vh}$ while conventional cross-hole tests produce a vertically polarised horizontally travelling shear wave $V_{S,hv}$ using a downhole vertical up–down hammer source, from which $G_{vh}$ and $G_{hv}$ can be calculated. However, horizontally polarised, horizontally travelling shear waves $V_{S,hh}$ have also been generated using a rotary cross-hole test (Butcher and Powell, 1996) equipped with a horizontal source-generating system as shown in figure 11, from which $G_{hh}$ can be determined [Clayton, 2011; Ku and Mayne, 2013]. Moreover, down-hole tests can be successfully integrated with seismic dilatometer test (SDMT) to detect the profiles of anisotropy ratio $G_{hh}/G_{hv}$ with depth, as discussed by Foti *et al.* [2006] for the clayey deposit at the site of Fucino in Italy. Ku and Mayne [2013] present a database of $V_S$ field measurements of well-documented sites in which the shear wave velocity $V_{S,hh}$ and at least one the quantities $V_{S,vh}$ and $V_{S,hv}$ are available. For the investigated clayey soils, $V_{S,vh} \approx V_{S,hv}$, while the component $V_{S,hh}$ is mostly greater than the previous two, revealing elastic stiffness anisotropy, especially for overconsolidated clays. The ratio $G_{hh}/G_{hv} > 1$ reflects the typical process of formation of clayey deposits and is consistent with the directional properties of the clay microstructure observed during one-dimensional consolidation in the laboratory, as discussed in Section 3.1.

All the above supports the idea that carrying out field wave propagation tests represents the most effective and less destructive mean to collect data aiming at initialising the porosity and fabric of a whole deposit, thus allowing a more rational and robust use of constitutive models based on such internal variables. It is in fact well known that the initialisation of the internal variables for the analysis of real engineering boundary value problems represents a challenging task, often far more complex than the calibration of the possibly numerous parameters of the model. The above

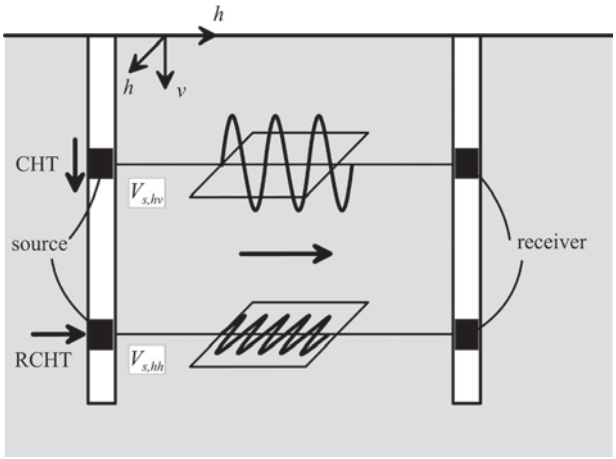


Fig. 11 – Scheme of seismic field tests: conventional cross-hole test (CHT) and rotary cross-hole test (RCHT).
*Fig. 11 – Schema di indagine sismica in sito: prove cross-hole convenzionali (CHT) e rotary cross-hole test (RCHT).*

discussion suggests a way to proceed, characterised by the complementary use of field wave propagation tests to initialise in detail the two internal variables, porosity and fabric, this paper is focusing on.

## 4. Thermodynamics with internal variables and its application to clays

Thermodynamics with internal variables (in the following TIV) is a framework used to describe the behaviour of complex materials by considering additional state variables that account for their internal structure and history. It tracks back to the pioneering work of COLEMAN and GURTIN [1967] and RICE [1971], as summarised in MAUGIN [2015]. In this approach, the internal variables can represent various aspects of the material such as microstructural features, damage accumulation, or deformation history, and they are treated as evolving quantities that are linked to the thermodynamic state variables through a set of evolution equations [MAUGIN, 1992].

The use of internal variables allows the modelling of complex material behaviour beyond the traditional framework of classical thermodynamics, which assumes that materials are in a state of local equilibrium and are characterized by a fixed set of thermodynamic state variables. By incorporating additional internal variables that describe the evolution of the material's internal structure or history, TIV can provide a more accurate description of materials that exhibit complex behaviour such as viscoelasticity, plasticity, or damage.

TIV has a wide range of applications in materials science, engineering, and physics, and it is used to model a variety of phenomena including fracture, fatigue, creep, and phase transformations. The framework is also useful for developing constitutive models for materials that undergo large deformations, exhibit hysteresis, or display nonlinear responses (*e.g.* MAUGIN and MUSCHIK, 1994).

The principles of thermodynamics with internal variables have been successfully adopted to formulate constitutive laws for geomaterials (*e.g.* HOULSBY, 1981; COLLINS and HOULSBY, 1997; HOULSBY and PUZRIN, 2006; EINAV, 2007; NGUYEN and EINAV, 2009; ROLLO and AMOROSI, 2020). Most of the above cited research works were developed in what is nowadays called hyperplasticity, that is a framework related to TIV. Fewer contributions to the geomechanics literature can be considered more strictly consistent to TIV, as developed within a rigorous convex analysis mathematical setting (*e.g.* NGUYEN, 2003; DE SIMONE and TAMAGNINI, 2004; HOULSBY and PUZRIN, 2006; ZOUAIN *et al.*, 2007, 2010; HJIAJ and DE SAXCÉ, 2008; HOULSBY, 2019; MARIGO and KAZYMYRENKO, 2019).

In the following, the general framework of TIV for clays is first briefly outlined, to then focus on the strategies to select the relevant internal variables and the potential functions, all inspired by the micro and macro features of clayey soils discussed in the previous sections. Two examples of the use of the approach to extend well-known hardening plasticity models for clays are finally proposed.

### *4.1. The general framework*

The TIV framework is only briefly summarised below. For a more detailed introduction please refer to the above quoted references.

Within TIV the constitutive behaviour is entirely defined by two potentials: the Helmholtz free energy $\varphi$ function and the (rate of) dissipation function $\dot{d}$. Limiting the following discussion to rate-independent fully saturated materials under isothermal conditions and assuming the additive decomposition:

$$\boldsymbol{\varepsilon}^e = \boldsymbol{\varepsilon} - \boldsymbol{\varepsilon}^p \tag{5}$$

The energy function will depend on the current elastic strain state $\boldsymbol{\varepsilon}^e$ and on a set of internal variables $\boldsymbol{\alpha}$ that, for clays can be defined as

$$\{\boldsymbol{\alpha}\} = \{v, \boldsymbol{\beta}\} \tag{6}$$

where $v$ is the specific volume of the material and $\boldsymbol{\beta}$ is a second order fabric tensor accounting for the orientation distribution of its particles or aggregates.

The energy function takes the form:

$$\varphi\left(\boldsymbol{\varepsilon}^e, \boldsymbol{\alpha}\right) = \varphi\left(\boldsymbol{\varepsilon}^e, v, \boldsymbol{\beta}\right) = \varphi\left(\boldsymbol{\varepsilon} - \boldsymbol{\varepsilon}^p, v, \boldsymbol{\beta}\right) \tag{7}$$

It is assumed to be convex and differentiable in $v$ and $\boldsymbol{\beta}$ and strictly convex in $\boldsymbol{\varepsilon}^e$. Taking its partial derivative with respect to the variables it results:

$$\boldsymbol{\sigma} = \frac{\partial \varphi}{\partial \boldsymbol{\varepsilon}^e};\ \overline{\chi}_v = -\frac{\partial \varphi}{\partial v};\ \overline{\boldsymbol{\chi}}_{\boldsymbol{\beta}} = -\frac{\partial \varphi}{\partial \boldsymbol{\beta}} \tag{8}$$

in which $\boldsymbol{\sigma}$ is the Cauchy effective stress tensor, $\overline{\chi}_v$ and $\overline{\chi}_\beta$ are the generalised stresses respectively associated to $v$ and $\boldsymbol{\beta}$, and:

$$\overline{\boldsymbol{\chi}}_{\boldsymbol{\varepsilon}^p} = -\frac{\partial \varphi}{\partial \boldsymbol{\varepsilon}^p} = \frac{\partial \varphi}{\partial \boldsymbol{\varepsilon}^e} = \boldsymbol{\sigma} \tag{9}$$

is the generalised stress associated to the plastic strain tensor, here equal to $\boldsymbol{\sigma}$.

The first and second principles of thermodynamics for isothermal processes can be expressed in the form:

$$\dot{\varphi} + \dot{d} = \boldsymbol{\sigma} : \dot{\boldsymbol{\varepsilon}}, \quad \dot{d} \geq 0 \tag{10}$$

where the first is known as the free energy balance equation, equating the rate of the mechanical work to that of the energy and dissipation functions, this latter being always greater than or equal to 0.

The rate of the Helmholtz free energy function is:

$$\dot{\varphi}\left(\boldsymbol{\varepsilon}^e, v, \boldsymbol{\beta}\right) = \frac{\partial \varphi}{\partial \boldsymbol{\varepsilon}^e} : \dot{\boldsymbol{\varepsilon}}^e + \frac{\partial \varphi}{\partial v}\dot{v} + \frac{\partial \varphi}{\partial \boldsymbol{\beta}} : \dot{\boldsymbol{\beta}} \tag{11}$$

which combined to equations (5) and (10) leads to:

$$\left[\frac{\partial \varphi}{\partial \boldsymbol{\varepsilon}^e} - \boldsymbol{\sigma}\right] : \dot{\boldsymbol{\varepsilon}}^e - \boldsymbol{\sigma} : \dot{\boldsymbol{\varepsilon}}^p + \frac{\partial \varphi}{\partial v}\dot{v} + \frac{\partial \varphi}{\partial \boldsymbol{\beta}} : \dot{\boldsymbol{\beta}} + \dot{d} = 0 \tag{12}$$

that holding also in absence of dissipative phenomena (*i.e.* $\dot{\boldsymbol{\varepsilon}}^p, \dot{v}, \dot{\boldsymbol{\beta}}, \dot{d}$ all equal to 0) confirms the state equation (8a). As such, the rate of dissipation takes the form:

$$\dot{d} = \dot{d}\left(\boldsymbol{\sigma}, v, \boldsymbol{\beta}, \dot{\boldsymbol{\varepsilon}}^p, \dot{v}, \dot{\boldsymbol{\beta}}\right) = \boldsymbol{\sigma} : \dot{\boldsymbol{\varepsilon}}^p + \overline{\chi}_v \dot{v} + \overline{\boldsymbol{\chi}}_{\boldsymbol{\beta}} : \dot{\boldsymbol{\beta}} \geq 0 \tag{13}$$

For a rate independent material the dissipation function is first order homogeneous in the rate of $\boldsymbol{\varepsilon}^p$, $v$ and $\boldsymbol{\beta}$. Consequently, according to the Euler's theorem, in the ideal case of a differentiable rate of dissipation it follows:

$$\dot{d} = \frac{\partial \dot{d}}{\partial \dot{\boldsymbol{\varepsilon}}^p} : \dot{\boldsymbol{\varepsilon}}^p + \frac{\partial \dot{d}}{\partial \dot{v}}\dot{v} + \frac{\partial \dot{d}}{\partial \dot{\boldsymbol{\beta}}} : \dot{\boldsymbol{\beta}} \geq 0 \tag{14}$$

where $\boldsymbol{\chi}_{\boldsymbol{\varepsilon}^p} = \partial \dot{d} / \partial \dot{\boldsymbol{\varepsilon}}^p$, $\chi_v = \partial \dot{d} / \partial \dot{v}$ and $\boldsymbol{\chi}_{\boldsymbol{\beta}} = \partial \dot{d} / \partial \dot{\boldsymbol{\beta}}$ are called dissipative generalised stress that, according to the orthogonality principle [Ziegler, 1977], are here assumed equal to the corresponding generalised stresses:

$$\boldsymbol{\chi}_{\boldsymbol{\varepsilon}^p} = \boldsymbol{\sigma},\ \chi_v = \overline{\chi}_v,\ \boldsymbol{\chi}_{\boldsymbol{\beta}} = \overline{\boldsymbol{\chi}}_{\boldsymbol{\beta}} \tag{15}$$

An element of complexity that characterises the application of TIV in the context of the material models discussed here is that they require non-differentiable rate of dissipations to reproduce the expected mechanical behaviour. For example, the rate of dissipation, which is first order homogeneous in $\dot{\boldsymbol{\varepsilon}}^p$, $\dot{v}$ and $\dot{\boldsymbol{\beta}}$, is not differentiable when these variables are all equal to zero. As such, instead of the above partial derivatives, the following more rigorous convex analysis-based definitions of the dissipative generalised stresses should be used:

$$\boldsymbol{\chi}_{\boldsymbol{\varepsilon}^p} \in \partial_{\dot{\boldsymbol{\varepsilon}}^p} \dot{d};\ \chi_v \in \partial_{\dot{v}} \dot{d};\ \boldsymbol{\chi}_{\boldsymbol{\beta}} \in \partial_{\dot{\boldsymbol{\beta}}} \dot{d} \tag{16}$$

in which the subgradients on the right side of the relationships define the sets each generalised dissipative stress belongs to (as indicated by the symbol $\in$), thus overpassing the limitation related to the non-differentiability of the rate of dissipation potential.

Again, relying on convex analysis tools, it is possible to switch from the rate of dissipation function to the corresponding yield domain that constrains the admissible states in the generalised stress space:

$$\mathbb{K} = \left\{ \left\{ \boldsymbol{\sigma}, v, \boldsymbol{\beta}, \boldsymbol{\chi}_{\boldsymbol{\varepsilon}^p}, \chi_v, \boldsymbol{\chi}_{\boldsymbol{\beta}} \right\} \middle| \overline{f}\left(\boldsymbol{\sigma}, v, \boldsymbol{\beta}, \boldsymbol{\chi}_{\boldsymbol{\varepsilon}^p}, \chi_v, \boldsymbol{\chi}_{\boldsymbol{\beta}}\right) \leq 0 \right\} \tag{17}$$

by obtaining its indicator function:

$$I_{\mathbb{K}} := \begin{cases} = 0, \text{ if } \left\{ \boldsymbol{\sigma}, v, \boldsymbol{\beta}, \boldsymbol{\chi}_{\boldsymbol{\varepsilon}^p}, \chi_v, \boldsymbol{\chi}_{\boldsymbol{\beta}} \right\} \in \mathbb{K} \\ + \infty, \text{ otherwise} \end{cases} \tag{18}$$

solving the following Legendre-Fenchel transform:

$$I_{\mathbb{K}} = \sup_{\left(\dot{\boldsymbol{\varepsilon}}^p, \dot{v}, \dot{\boldsymbol{\beta}}\right)} \left\{ \boldsymbol{\chi}_{\boldsymbol{\varepsilon}^p} : \dot{\boldsymbol{\varepsilon}}^p + \chi_v \dot{v} + \boldsymbol{\chi}_{\boldsymbol{\beta}} : \dot{\boldsymbol{\beta}} - \dot{d}\left(\boldsymbol{\sigma}, v, \boldsymbol{\beta}, \dot{\boldsymbol{\varepsilon}}^p, \dot{v}, \dot{\boldsymbol{\beta}}\right) \right\} \tag{19}$$

in which $\boldsymbol{\sigma}, v, \boldsymbol{\beta}$ play the role of passive variables in the search for the least upper bound of the set in braces operated by the supremum (sup).

A key result of convex analysis (see for example Han and Reddy, 1999) is the normality rule that holds in the generalised stress space, leading to evolution laws for the internal variables that, in the case of a differentiable function $\overline{f}$, result as:

$$\dot{\boldsymbol{\varepsilon}}^p = \dot{\gamma}\frac{\partial \overline{f}}{\partial \boldsymbol{\chi}_{\boldsymbol{\varepsilon}^p}};\quad \dot{v} = \dot{\gamma}\frac{\partial \overline{f}}{\partial \chi_v};\quad \dot{\boldsymbol{\beta}} = \dot{\gamma}\frac{\partial \overline{f}}{\partial \boldsymbol{\chi}_{\boldsymbol{\beta}}} \tag{20}$$

in which $\dot{\gamma} \geq 0$ is the plastic multiplier of the classical plasticity theory.

As a final step, it is worth establishing the corresponding yield criterion in the Cauchy stress space, expressing $\overline{f}$ as a function of $\boldsymbol{\sigma}, v, \boldsymbol{\beta}$ via equation (15) and equation (8), obtaining the more familiar:

$$f\left(\boldsymbol{\sigma}, v, \boldsymbol{\beta}\right) \leq 0 \tag{21}$$

At this stage the whole structure of a single surface hardening plasticity model is recovered, though derived within a more general theoretical setting. This latter offers the advantage of ensuring that the formulation does not violate the principles of thermodynamics and, at the same time, consistently accounts for the possibly more comprehensive couplings between different aspects of the mechanics of the studied material, as will be briefly illustrated in the two final examples of this section.

### *4.2. Micro-inspired selection of internal variables and potential functions*

As previously anticipated, internal variables are meant to represent the average microstructural features that control the macroscopic mechanical behaviour of the material. By definition, internal variables should in principle be measurable while not being controllable: their evolution is driven by energy dissipation, as represented in equation (14) in which to each internal variable corresponds a generalised stress acting on its rate. The number of internal variables should be kept as small as possible but sufficient to describe the key features of the material.

In light of what discussed in Section 2, in the case of reconstituted or soft clays a first attempt to describe their mechanical behaviour should involve, as internal variables, the inter-aggregates porosity, or any equivalent scalar as the specific volume $v$, a tensor-valued fabric descriptor, as the second order symmetric tensor $\boldsymbol{\beta}$ accounting for the orientation distribution of the aggregates, and the plastic strain tensor $\boldsymbol{\varepsilon}^p$, to describe the frictional behaviour stemming from the mutual interacions between aggregates of particles. This latter variable will only enter the formulation by its rate, to avoid the conceptual limitation related to the impossibility of performing a direct measurement of the plastic strain cumulated by a natural material in its geological history, along the line discussed in RUBIN [2001].

In detail, specific volume and its rate are defined as:

$$v = \frac{V}{V_s}; \quad \frac{\dot{v}}{v} = \frac{\dot{V}}{V} - \frac{\dot{V}_s}{V_s} \tag{22}$$

where $V$ is the total volume and $V_s$ the volume of the solids. Recalling the definition of the total volumetric strain rate ($\dot{\varepsilon}_v = -\dot{V}/V$), assuming the additive decomposition of elastic and plastic strains and, according to COLLINS *et al.* [2010], identifying the elastic volumetric strain rate as the variation of the solids volume, it results:

$$\dot{\varepsilon}_v^e = -\frac{\dot{V}_s}{V_s}; \quad \dot{\varepsilon}_v^p = -\frac{\dot{v}}{v} \tag{23}$$

This assumption, originally proposed for granular materials, can also be adopted for clays based on the hypothesis that aggregates of particles mainly deform elastically, as for example discussed in PEDROTTI and TARANTINO [2018]. Equation (23) implies that the specific volume can be adopted as suitable internal variable within the thermodynamic constitutive framework to describe the dissipative processes involved in permanent modifications of the porosity in clays. It is worth noting that, differently from ROLLO and AMOROSI [2022], here the specific volume is adopted instead of the preconsolidation pressure $p_c$. Nonetheless, the two variables can be related by:

$$\dot{p}_c = -\frac{p_c}{\lambda^*}\frac{\dot{v}}{v}; \quad p_c = p_r\left(\frac{v}{N}\right)^{-\frac{1}{\lambda^*}} \tag{24}$$

where $N$ is the specific volume at the reference pressure $p_r$ and $\lambda^*$ the parameter governing the isotropic hardening law in the Cam clay-family plasticity models.

The other internal variable $\boldsymbol{\beta}$ is a second order fabric tensor accounting for the orientation distribution of the aggregates. In the following, its evolution is assumed to be related to plastic strain rates, according to the distortional hardening law proposed by ROLLO & AMOROSI (2022):

$$\dot{\boldsymbol{\beta}} = c\left(\boldsymbol{\beta}_b - \boldsymbol{\beta}\right)\sqrt{\left(\dot{\varepsilon}_v^p + \boldsymbol{\beta} : \dot{\boldsymbol{\varepsilon}}'^p\right)^2 + \frac{2}{3}\left(M^2 - \beta^2\right)\dot{\boldsymbol{\varepsilon}}'^p : \dot{\boldsymbol{\varepsilon}}'^p} \tag{25}$$

where $M$ is the stress ratio at critical state and $\boldsymbol{\varepsilon}'^p$ the deviatoric plastic strain tensor. $\beta$ is the triaxial counterpart of $\boldsymbol{\beta}$ , $\beta = \sqrt{3/2\,\boldsymbol{\beta} : \boldsymbol{\beta}}$, $c$ is a parameter controlling the pace of the evolution and $\boldsymbol{\beta}_b$ represents the equilibrium "bounding" value towards which $\boldsymbol{\beta}$ tends to, function of the current stress ratio $\mathbf{r}=\mathbf{s}/p$, with $\mathbf{s}$ deviatoric part of the effective stress, for which different expressions have been provided in the literature (*e.g.* DAFALIAS and TAIEBAT, 2013).

The selection of the energy function is pursued by analysing the experimental observations of wave propagations carried out at different states of the material. In detail, the starting point of the process is that of assuming for the energy function the general expression of equation (7), such that:

$$\boldsymbol{\sigma} = \frac{\partial \varphi\left(\boldsymbol{\varepsilon}^e, v, \boldsymbol{\beta}\right)}{\partial \boldsymbol{\varepsilon}^e} \tag{26}$$

and, after differentiation:

$$\dot{\boldsymbol{\sigma}} = \frac{\partial^2 \varphi\left(\boldsymbol{\varepsilon}^e, v, \boldsymbol{\beta}\right)}{\partial \boldsymbol{\varepsilon}^e \otimes \partial \boldsymbol{\varepsilon}^e} : \dot{\boldsymbol{\varepsilon}}^e + \frac{\partial^2 \varphi\left(\boldsymbol{\varepsilon}^e, v, \boldsymbol{\beta}\right)}{\partial \boldsymbol{\varepsilon}^e \partial v}\dot{v} + \frac{\partial^2 \varphi\left(\boldsymbol{\varepsilon}^e, v, \boldsymbol{\beta}\right)}{\partial \boldsymbol{\varepsilon}^e \otimes \partial \boldsymbol{\beta}} : \dot{\boldsymbol{\beta}} \tag{27}$$

The first term on the right side of equation (27) is the fourth order reversible stiffness tensor, which is the only one detected during wave propagation tests, as the perturbations induced in the soil are small enough not to determine any instantaneous variation of the specific volume ($\dot{v} = 0$) and of the fabric tensor ($\dot{\boldsymbol{\beta}} = 0$). As such, this can be interpreted as

an instantaneous picture of the response of the soil, depending on the energy content via its current state, *i.e.* $\boldsymbol{\varepsilon}^e$, or its dual $\boldsymbol{\sigma}$, $v$ and $\boldsymbol{\beta}$. In the laboratory experiments discussed in Section 3, wave propagation tests were carried out at different states, providing a comprehensive data set, sufficient to back-evaluate an analytical expression for the energy function of equation (7), as discussed in HOULSBY *et al.* [2005, 2019] and in AMOROSI *et al.* [2020].

For what concerns the selection of the dissipation function, the following assumptions have been adopted. First of all, the function has to be homogeneous of degree one in the rates $\dot{\boldsymbol{\varepsilon}}^p$, $\dot{v}$ and $\dot{\boldsymbol{\beta}}$, aiming at considering a rate-independent behaviour. Furthermore, it has to be strictly positive for non-zero values of the above rates and equal to zero when the rates are zero. The structure of the rate of dissipation functions adopted in the following examples is inspired by the pioneering work of HOULSBY [1981] and its extension discussed in COLLINS and HOULSBY [1997], in which for a Cam-Clay family model the following function was proposed:

$$\dot{d}\left(\dot{\varepsilon}_v^p, \dot{\varepsilon}_s^p, p_c\right) = \frac{p_c}{2}\left(\sqrt{\dot{\varepsilon}_v^{p2} + M^2\dot{\varepsilon}_s^{p2}} + \dot{\varepsilon}_v^p\right) \qquad (28)$$

where the square root term, an Euclidean norm of the volumetric and weighted deviatoric plastic strain rates ($\varepsilon_s = \sqrt{2/3\boldsymbol{\varepsilon}' : \boldsymbol{\varepsilon}'}$), is scaled by half of the preconsolidation pressure $p_c$. This leads to a pseudo-frictional material whose dissipative response does not depend on the mean effective pressure, as customary in coarse-grained soils, but on $p_c$, here tracking the permanent evolution of the porosity of the clay. The last term in the expression provides a shift of the resulting yield domain in the generalised stress space: it represents an alternative option as compared to the one originally proposed by HOULSBY [1981], where such a term is absent in the dissipation function but appears, once integrated in time, as an additional term in the energy function. A general discussion on the implications of the above two alternative options is beyond the scope of this paper: the interested reader can refer to GURTIN and REDDY [2009] and to the more recent ULLOA *et al.* [2021] for further details.

The dissipation functions adopted in the following examples result from equation (28), introducing the necessary specific modifications that are commented in detail in the following.

### *4.3. Example 1: a revised Modified Cam-Clay model*

This first example consists of an updated version of the well-known Modified Cam-Clay model, in which the key mechanical modifications are inspired by some of the experimental results discussed in Sections 2 and 3. Here the specific volume is assumed as the internal variable tracking the past history of the material: it appears explicitly in the energy function, such that this function not only accounts for the non-linear dependence of the stiffness on the current stress (or elastic strain) state, following HOULSBY *et al.* [2005], but also depends on the current specific volume, resulting in:

$$\varphi\left(\varepsilon_v^e, \varepsilon_s^e, v\right) = \left(\frac{v}{N}\right)^{\frac{r}{(n-1)\lambda^*}} \left\{\frac{p_r}{k\left(2-n\right)} k^{\frac{2-n}{1-n}} \left(1-n\right)^{\frac{2-n}{1-n}} \left[\varepsilon_v^{e2} + \frac{3g}{k\left(1-n\right)}\varepsilon_s^{e2}\right]^{\frac{2-n}{2-2n}}\right\} \qquad (29)$$

in which $n$, $k$ and $g$ are the parameters of the hyperelastic potential of HOULSBY *et al.* [2005], here in braces, scaled by the specific volume function via the parameter $r$. All these parameters can be easily calibrated based on shear wave propagation experiments.

For what concerns the rate of dissipation the following expression is here adopted:

$$\dot{d}\left(\dot{\varepsilon}_v^p, \dot{\varepsilon}_s^p, \dot{v}, v\right) = \frac{p_r}{2}\left(\frac{v}{N}\right)^{-\frac{1}{\lambda^*}}\left(\sqrt{\dot{\varepsilon}_v^{p2} + M^2\dot{\varepsilon}_s^{p2}} + \dot{\varepsilon}_v^p\right) + I_{\mathbb{K}}\left(\frac{\dot{v}}{v} + \dot{\varepsilon}_v^p\right) \qquad (30)$$

in which the preconsolidation pressure of equation (28) is replaced by its specific volume counterpart based on equation (24b). Furthermore, the last term is an indicator function imposing as a constraint the fundamental assumption of equation (23b) such that:

$$I_{\mathbb{K}[0,0]} := \begin{cases} = 0, \text{ if } \left(\dfrac{\dot{v}}{v} + \dot{\varepsilon}_v^p\right) \in \mathbb{K} \rightarrow -\dfrac{\dot{v}}{v} = \dot{\varepsilon}_v^p \\ + \infty, \text{ otherwise} \end{cases} \qquad (31)$$

By standard application of the convex analysis-based procedure previously illustrated, the above rate of dissipation leads to the following yield domain in the generalised stress space:

$$\overline{f} = \chi_q^2 + M^2\left(\chi_p - v\chi_v\right)\left[\chi_p - v\chi_v - p_r\left(\frac{v}{N}\right)^{-\frac{1}{\lambda^*}}\right] \leq 0 \qquad (32)$$

and to the corresponding yield domain $f$ in the Cauchy stress space, represented in figure 12.

One of the key features of this isotropic formulation is the intrinsic coupling of the energy and dissipation functions, both dependent on the internal variable $v$. This not only implies the dependence of the reversible behaviour on the previously experienced irreversible history, tracked by the specific volume, but also makes the irreversible behaviour affected by the above coupling, resulting in a non-associated flow response in the Cauchy stress space. This is illustrated in figure 12 with reference to four triaxial undrained simulations carried out at different overconsolidation ratios, whose stress-strain curves are also shown in the figure, with the deviatoric stress $q = \sqrt{3/2\,\mathbf{s} : \mathbf{s}}$. Tests

were carried out with reference to the relevant parameters of Set 1 in table I.

### 4.4. Example 2: a revised Saniclay model

In this section a TIV-based anisotropic model for clays is proposed. It can be considered as an extension of the formulations proposed by DAFALIAS *et al.* [2006] and by DAFALIAS and TAIEBAT [2013], all belonging to the family of simple anisotropic clay plasticity models (Saniclay).

Here both the specific volume and the fabric tensor are assumed as internal variables tracking the past history of the material: they appear explicitly in the energy potential, such that this function accounts for the non-linear dependence of the stiffness on the current effective stress (or elastic strain) state, following HOULSBY *et al.* [2019] and AMOROSI *et al.* [2020]. It also depends on the current values of the specific volume and fabric tensor, resulting in:

$$\varphi\left(\boldsymbol{\varepsilon}^e, v, \boldsymbol{\beta}\right) = \left(\frac{v}{N}\right)^{\frac{r}{(n-1)\lambda^*}} \frac{p_r}{k\left(2-n\right)} k^{\frac{2-n}{1-n}} \left(1-n\right)^{\frac{2-n}{1-n}} \left\{\left[k\left(1-n\right)-\frac{2}{3}g\right]\mathrm{tr}^2\left(\boldsymbol{\varepsilon}^e-\omega\beta\boldsymbol{\beta}\boldsymbol{\varepsilon}^e\right)+2g\,\mathrm{tr}\left[\left(\boldsymbol{\varepsilon}^e-\omega\beta\boldsymbol{\beta}\boldsymbol{\varepsilon}^e\right)^2\right]\right\}^{\frac{2-n}{2-2n}} \tag{33}$$

where $\omega$ is an additional model parameter controlling the intrinsic tendency of the clay to develop anisotropy, which can be estimated as a function of its plasticity index [AMOROSI *et al.*, 2021].

The dissipation function proposed for this model is the following:

$$\dot{d}\left(v, \boldsymbol{\beta}, \dot{\boldsymbol{\varepsilon}}^p, \dot{v}, \dot{\boldsymbol{\beta}}\right) = \frac{p_r}{2}\left(\frac{v}{N}\right)^{-\frac{1}{\lambda^*}} \left(\dot{\bar{d}} + \dot{\varepsilon}_v^p + \boldsymbol{\beta}:\dot{\boldsymbol{\varepsilon}}'^p\right) + + I_{\mathbb{K}}\left(\frac{\dot{v}}{v} + \dot{\varepsilon}_v^p\right) + I_{\mathbb{L}}\left[\dot{\boldsymbol{\beta}} - c\left(\boldsymbol{\beta}_b - \boldsymbol{\beta}\right)\dot{\bar{d}}\right] \tag{34}$$

with

$$\dot{\bar{d}} = \sqrt{\left(\dot{\varepsilon}_v^p + \boldsymbol{\beta}:\dot{\boldsymbol{\varepsilon}}'^p\right)^2 + \frac{2}{3}\left(M^2 - \beta^2\right)\dot{\boldsymbol{\varepsilon}}'^p:\dot{\boldsymbol{\varepsilon}}'^p} \tag{35}$$

Tab. I – Model parameters for the tested soils.
*Tab. I – Parametri del modello per i terreni analizzati.*

| Parameters | Values | |
|---|---|---|
| | Set 1 | Set 2 |
| $p_r$ (kPa) | 100 | 100 |
| $k$ | 67 | 67 |
| $g$ | 50 | 50 |
| $n$ | 0.8 | 0.8 |
| $N$ | 1.8 | 1.8 |
| $r$ | 0.4 | 0.4 |
| $M$ | 1.0 | 1.0 |
| $\lambda^*$ | 0.07 | 0.07 |
| $\omega$ | - | 1.5 |
| $c$ | - | 30 |
| $z$ | - | 2.5 |
| $s$ | - | 5.0 |

and

$$I_{\mathbb{L}[0,0]} := \begin{cases} = 0, \text{ if } \left[\dot{\boldsymbol{\beta}} - c\left(\boldsymbol{\beta}_b - \boldsymbol{\beta}\right)\dot{\bar{d}}\right] \in \mathbb{L} \rightarrow \dot{\boldsymbol{\beta}} = c\left(\boldsymbol{\beta}_b - \boldsymbol{\beta}\right) \\ + \infty, \text{ otherwise} \end{cases} \tag{36}$$

Comparing equations (30) to (34) it clearly emerges that the former is formulated in terms of direct invariants of the rate of plastic strain, given the isotropic character of the model, while this is not possible for the latter, as aimed at accounting for anisotropy. Furthermore, in the proposed anisotropic rate of dissipation, the term $\dot{\bar{d}}$ is again an Euclidean norm now explicitly dependent on the fabric tensor $\boldsymbol{\beta}$, leading to distorted yield domain in the generalised stress space and, consequently, in the Cauchy one. Finally, the two indicator functions $I_{\mathbb{K}}$ and $I_{\mathbb{L}}$ act as constraints to ensure that equation (23) and equation (25) are satisfied in the irreversible regime.

A series of tests have been simulated to highlight some of the features of this extended Saniclay model, all based on the parameters of Set 2 reported in

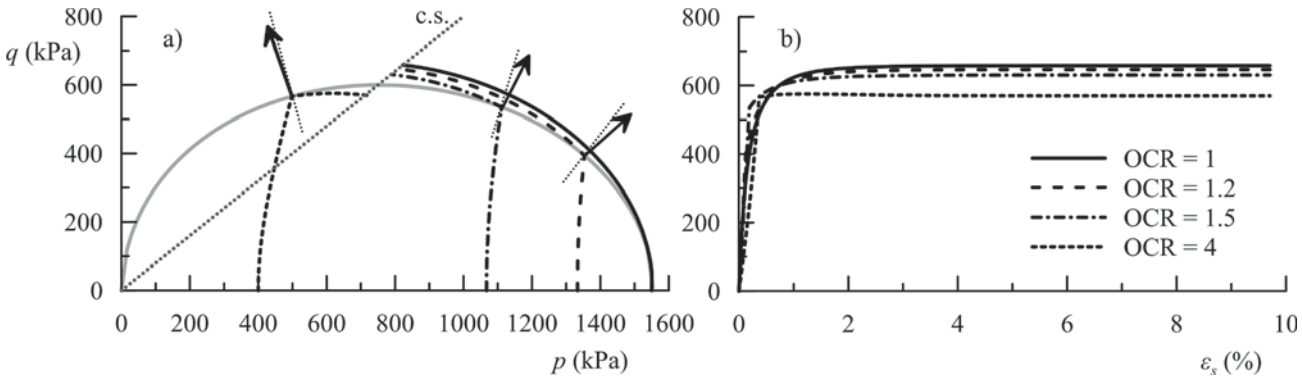


Fig. 12 – Revised Modified Cam-Clay model: a) initial yield domain and stress paths; b) stress-strain response.
*Fig. 12 – Rivisitazione del modello di Cam-Clay modificato: a) superficie di snervamento iniziale e percorsi tensionali; b) curve sforzi-deformazioni.*

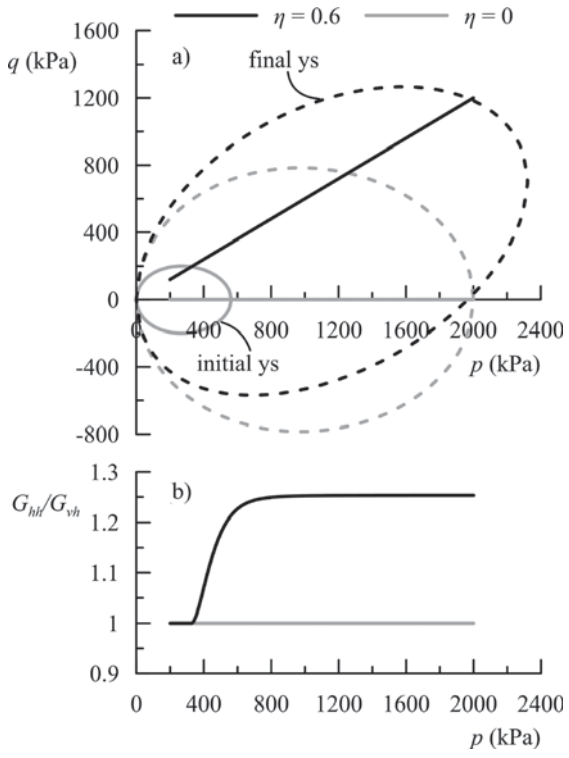


Fig. 13 – Radial stress paths and related evolution of the stiffness anisotropy ratio.
*Fig. 13 – Percorsi tensionali radiali e relativa evoluzione del rapporto di anisotropia.*

table I. In all the test simulations the following expression for $\boldsymbol{\beta}_b$ was adopted [DAFALIAS and TAIEBAT, 2013]:

$$\boldsymbol{\beta}_b = \sqrt{\frac{2}{3}}\frac{M}{z}\left[1-\exp\left(-s\frac{|\eta|}{M}\right)\right]\frac{\mathbf{r}}{\|\mathbf{r}\|} \qquad (37)$$

in which:

$$\mathbf{r} = \frac{\mathbf{s}}{p}; \quad \|\mathbf{r}\| = \sqrt{\mathbf{r}:\mathbf{r}}; \quad |\eta| = \sqrt{\frac{3}{2}\mathbf{r}:\mathbf{r}} \qquad (38)$$

leading to a non-linear dependence of $\boldsymbol{\beta}_b$ on the current direction of the stress path as expressed by its generalised stress ratio. Figure 13 illustrates the results of two constant radial triaxial stress path tests, respectively characterised by $\eta$ equal to 0 (isotropic) and 0.6, applied to the same initially isotropic clay, characterised by $p$ = 200 kPa and $v$ = 1.633. The model predicts a different evolution of the yield surface, which in both cases expands due to the reduction of the specific volume, while keeping centred in the case of the isotropic path or experiencing a substantial distortion in the $\eta$ = 0.6 case. This is related to the different evolution of the fabric tensor $\boldsymbol{\beta}$ in the two tests, which reflects into the corresponding different evolution of the stiffness anisotropy ratio, also shown in figure 13. Those patters resemble what observed by MITARITONNA *et al.* [2014], as discussed in Section 3.

Moreover, a series of undrained triaxial tests were simulated after imposing a virgin radial loading along the $\eta$ = 0.6 stress path followed, in two cases, by a radial unloading prior to the shearing stage. The results are illustrated in figure 14 in terms of undrained stress paths, stress-strain curves, and evolution of the stiffness anisotropy ratio: it results that during the simulated shearing stages the clay does not experience significant fabric evolution, as confirmed by the minor modifications observed in terms of stiffness anisotropy ratio.

Finally, ideal undrained simple shear tests were performed to highlight the tensorial character of the anisotropic coupling and to figure out the model response along a stress path that induces a rotation of the principal directions of the stress and

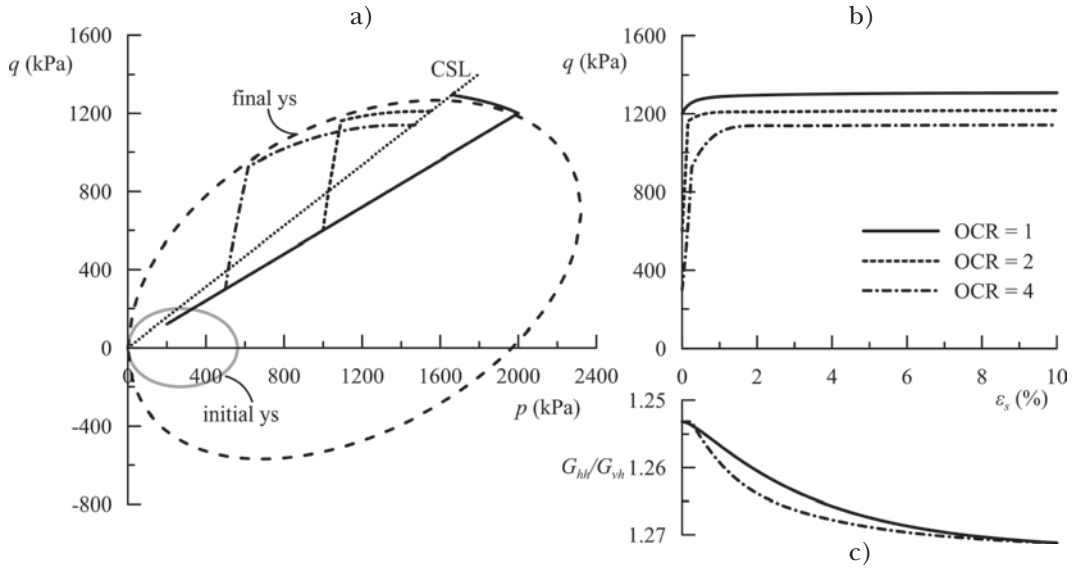


Fig. 14 – Revised Saniclay model: a) initial yield domain and stress paths; b) stress-strain response and c) evolution of the elastic stiffness anisotropy ratio.
*Fig. 14 – Modello Saniclay rivisitato: a) superficie di snervamento iniziale e percorsi tensionali; b) curve sforzi-deformazioni e c) evoluzione del rapporto di anisotropia elastica.*

fabric tensors. The shearing stage follows the radial loading and unloading at $\eta = 0.6$ stress from $p = 2000$ kPa (OCR = 1) and $p = 1000$ kPa (OCR = 2). Shear strain ($\gamma$) controlled simulations along the horizontal direction are carried out adopting the Set 2 of model parameters of table I, leading to the rise of shear stress $\tau$ as shown in figure 15. Since the test is performed under plane strain conditions, the normal stress component orthogonal to the plane of shearing is always a principal one, while a rotation of the principal directions of $\boldsymbol{\sigma}$ and $\boldsymbol{\beta}$ occurs in the shearing plane and can be quantified through the angle $\alpha$ with respect to the horizontal direction as sketched in figure 15. The principal values (*i.e.* eigenvalues) of $\boldsymbol{\beta}$ are also computed. As the proposed formulation does not depend on the Lode angle, during the shearing phase the horizontal stress components $\sigma_h$ acting on the constrained (*i.e.* vertical) planes evolve until they equate the vertical one $\sigma_v$ at critical state. This process involves a rotation of the principal directions of $\boldsymbol{\sigma}$ from the initial triaxial configuration ($\alpha = 0°$) until the final value $\alpha = 45°$. A similar, though delayed trend governed by the plastic process is observed for $\boldsymbol{\beta}$: the principal directions of the fabric tensor coincide with the horizontal and vertical ones as long as the response is elastic but when the yield surface is reached they start rotating towards the value of 45°. Not surprisingly, when $\boldsymbol{\beta}$ reaches the bounding value, the stress and fabric tensor become coaxial as $\boldsymbol{\beta}_b$ is proportional to the deviatoric stress. Therefore, at the end of the process only the shear-like component of $\boldsymbol{\beta}$ related to the shear stress is non-zero and, consistently, the maximum and minimum eigenvalues have the same magnitude but opposite sign (Fig. 15b).

Figure 15c reveals that the elasto-plastic coupling keeps track of the evolution of the elastic stiffness anisotropy during the loading process. Specifically, the increase of the shear-like component of $\boldsymbol{\beta}$ leads to an increase of shear modulus $G_{hv}$ and a consequent reduction of the ratio $G_{hh}/G_{hv}$. The magnitude of the shear moduli depends on the fabric evolution as well as on the current stress by virtue of the nonlinear hyperelastic formulation. In fact, equation (33) takes into account both the microstructure-related anisotropy, via the fabric tensor $\boldsymbol{\beta}$, and the so-called 'stress-induced anisotropy', determined by the instantaneous force chains generated within the material and macroscopically reflected into its non-linear elastic response.

Therefore, the results obtained for $n = 0$ (linear elasticity) are also shown to isolate the contribution of the fabric (*i.e.* inherent) anisotropy. Comparison between figure 14c and figure 15c indicates that different values of $G_{hh}/G_{hv}$ are reached at critical state depending on the loading path. In fact, the model requires the invariance of $\beta$ (*i.e.* the

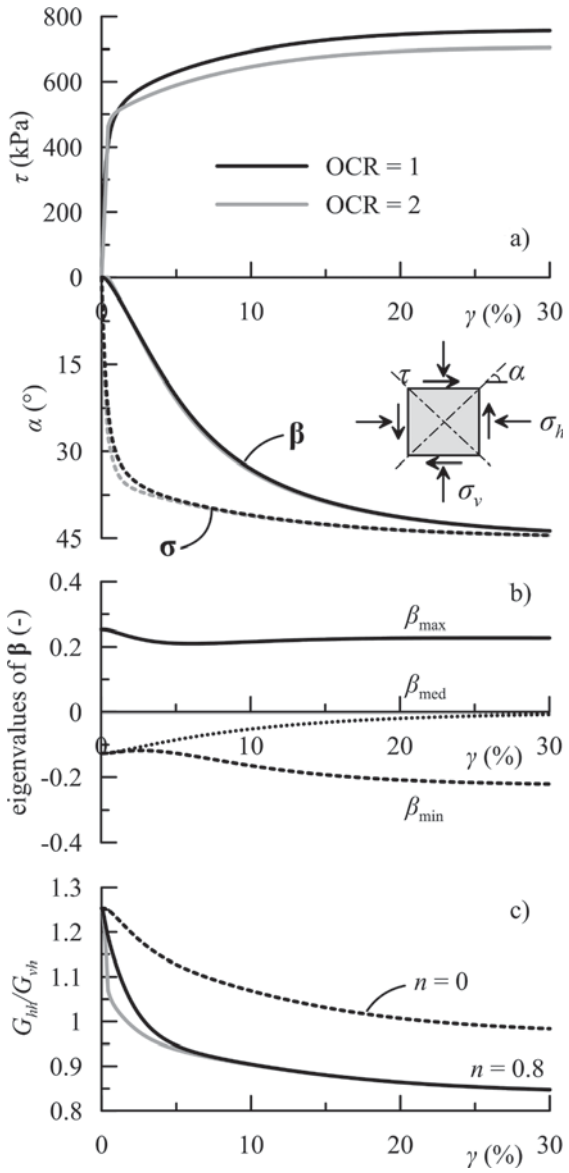


Fig. 15 – Revised Saniclay model: simulations of undrained simple shear tests in terms of a) stress-strain curves; b) principal directions and eigenvalues of $\boldsymbol{\beta}$ and c) evolution of the elastic stiffness anisotropy ratio.

*Fig. 15 – Modello Saniclay rivisitato: simulazioni di prove di taglio semplice non drenate in termini di a) curve sforzi-deformazioni; b) direzioni principali e autovalori di $\boldsymbol{\beta}$ e c) evoluzione del rapporto di anisotropia elastica.*

norm of the fabric tensor $\boldsymbol{\beta}$) at critical state, that does not exclude the possibility of having different components of the fabric tensor, and hence different asymptotic anisotropy ratios according to the stress path. Naturally, at this point one question arises: should the critical state be anisotropic and if so, should the stiffness anisotropy be dependent on the followed stress path and the final stress configuration? There is no definitive answer to this question, which is still a debated issue among the geomechanics community. However, for granular ma-

terials the idea of an anisotropic critical state [Dafalias, 2016] is getting gradually more attractive as supported by preliminary experimental observations [Zhao *et al.,* 2021] and discrete element analyses [Wang *et al.,* 2020]. For clays the trend is less clear but microstructural investigations that combine scanning electron microscopy and X-ray microtomography [Gao *et al.,* 2020] suggest that the clusters of particles tend to assume a more iso-oriented arrangement according to the applied state of stress when approaching the critical state. However, despite the open challenge of experimentally exploring the behaviour of the clay in this configuration, the identification of an anisotropic form of elastic-plastic coupling may justify the use of reversible regime data as a proxy for detecting the fabric anisotropy at critical state.

## 5. Conclusions and future developments

Clays are ubiquitous in geotechnical and environmental engineering applications and understanding their complex mechanical behaviour is essential for designing and constructing safe and efficient structures.

Over the years, numerous constitutive models have been developed to describe their mechanical behaviour, but only few of them were formulated taking into account the complex microstructural behaviour of these materials.

Recently, there has been a growing interest in micro-inspired constitutive modelling of clays, which seeks to incorporate microscale processes and properties into macroscopic constitutive models. This approach involves understanding the micromechanical behaviour of clays, including the role of particle/aggregate porosity and fabric evolution, using this knowledge to develop macroscopic models that capture the behaviour of these materials. Micro-inspired constitutive modelling has the potential to improve the accuracy and reliability of constitutive models for clays and ultimately lead to safer and more efficient geotechnical and environmental engineering practices.

The aim of this paper is to provide an overview of some recent advances in micro-inspired constitutive modelling of clays. After a review of multi-scale experimental evidences and their possible interpretation and generalisation in terms of internal variables controlling the mechanics of clayey soils, two examples of constitutive models were proposed, both developed in the framework of thermodynamics with internal variables. This theoretical environment allows the effective development of constitutive models that not only respect the fundamental principles of thermodynamics, but also directly benefit from our understanding of the complex micromechanics of clayey soils.

The ongoing development of new and more accurate experimental tools, providing quantitative insights into the micromechanics of clays, together with the parallel development of DEM-based numerical models, specifically formulated for these complex materials (*e.g.* Pagano *et al.*, 2020), represent a promising context for the development of future research, aimed at bridging the gap between the micro- and macro-scale in clay soils.

## Acknowledgements

This study was carried out within the RETURN Extended Partnership and received funding from the European Union Next-GenerationEU (National Recovery and Resilience Plan – NRRP, Mission 4, Component 2, Investment 1.3 – D.D. 1243 2/8/2022, PE0000005).

## Notation

$c$ RH parameter
$\dot{d}$ Rate of dissipation
$e$ Void ratio
$\overline{f}$ Yield function in generalised stress space
$f$ Yield function in stress space
$\mathbf{F}$ Fabric tensor
$g$ Dimensionless shear modulus coefficient
$G_0$, $G_{hh}$, $G_{hv}$ Elastic shear modulus
$I$ Indicator function
$k$ Dimensionless bulk modulus coefficient
$K_0$ Earth pressure coefficient
$l$ Vector length
$\overline{L}$ Dispersion index
$M$ Critical stress ratio
$n$ Exponent in power-law relationship for elastic stiffness
$\mathbf{n}$ Direction of particles/aggregates
OCR Overconsolidation ratio
$p$ Mean effective stress
$p_c$ Preconsolidation pressure
$p_r$ Reference pressure
$q$ Deviatoric stress
$r$ Parameter of equation (29)
$\mathbf{r}$ Stress ratio tensor
$s$ RH parameter of equation (37)
$\mathbf{s}$ Deviatoric part of the stress tensor
$v$ Specific volume
$V$ Total volume
$V_s$ Solid volume, shear wave velocity
$z$ RH parameter of equation (37)
$\boldsymbol{\alpha}$ Internal variable tensor
$\boldsymbol{\beta}$ Rotational hardening variable
$\boldsymbol{\beta}_b$ Bound of $\beta_{ij}$

$\beta$ Rotational hardening variable in $p$-$q$ plane
$\beta_b$ Bound of $\beta$ in $p$-$q$ plane
$\gamma$ Shear strain
$\dot{\gamma}$ Plastic multiplier
$\boldsymbol{\varepsilon}$ Strain tensor
$\varepsilon_s$ Deviatoric strain invariant
$\varepsilon_v$ Volumetric strain
$\eta$ Stress ratio
$\vartheta$ Particles direction
$\lambda^*$ Isotropic hardening parameter
$\boldsymbol{\sigma}$ Stress tensor
$\tau$ Shear stress
$\varphi$ Helmholtz free energy, friction angle
$\overline{\boldsymbol{\chi}}, \overline{\boldsymbol{\chi}}_\beta, \overline{\chi}_v$ Generalised stresses
$\overline{\chi}_p, \overline{\chi}_q$ Generalised stresses in triaxial formulation
$\boldsymbol{\chi}$ Dissipative generalised stress tensor
$\chi_p, \chi_q$ Dissipative generalised stresses in triaxial formulation
$\omega$ Parameter of equation (33)

## References


AMOROSI A., ROLLO F., DAFALIAS Y.F. (2021) – *Relating elastic and plastic fabric anisotropy of clays.* Géotechnique, 71, n.7, pp. 583-593.

AMOROSI A., ROLLO F., HOULSBY G.T. (2020) – A *nonlinear anisotropic hyperelastic formulation for granular materials: comparison with existing models and validation.* Acta Geotechnica, 15, pp. 179-196.

ANANDARAJAH A. (2000a) – *Numerical simulation of one-dimensional behavior of a kaolinite.* Géotechnique**,** 50, n**.** 5, pp. 509-519.

ANANDARAJAH A. (2000b) – *On influence of fabric anisotropy on the stress-strain behavior of clays.* Computers and Geotechnics, 27, pp. 1-17.

BARDEN L., SIDES G.R. (1970) – *Engineering behavior and structure of compacted clay.* Journal of the Soil Mechanics and Foundations Division, 96, n. 4, pp. 1171-1200.

BUTCHER A. P., POWELL J. J. M. (1996) – *Practical considerations for field geophysical techniques used to assess ground stiffness.* Proc. Int. Conf. on Advances in Site Investigation Practice, Institution of Civil Engineers, Telford, London, pp. 701-714.

CALLISTO L., CALABRESI G. (1998) – *Mechanical behaviour of a natural soft clay.* Géotechnique, 48, n. 4, pp. 495-513.

CETIN H. (2004) – *Soil-particle and pore orientations during consolidation of cohesive soils.* Engineering geology, 73, nn.1-2, pp. 1-11.

CHANG C.S., HICHER P.Y., YIN Z.Y., KONG L.R. (2009) – *Elastoplastic model for clay with microstructural consideration.* Journal of engineering mechanics, 135, n. 9, pp. 917-931.

CHOW J.K., LI Z., WANG Y.H. (2019) – *Comprehensive microstructural characterizations of 1-D consolidated kaolinite samples with fabric tensors and pore elongation factors.* Engineering Geology, 248, pp. 22-33.

CLAYTON C.R.I. (2011) – *Stiffness at small strain: research and practice.* Géotechnique, 61, n. 1, pp. 5-37.

COLEMAN B.D, GURTIN M.E. (1967) – *Thermodynamics with internal state variables.* J.Chem. Phys. 47, pp. 597-613.

COLLINS I.F., HOULSBY G.T. (1997) – *Application of thermomechanical principles to the modelling of geotechnical materials.* Proceedings of the Royal Society of London. Series A: Mathematical, Physical and Engineering Sciences, 453, pp. 1975-2001.

COLLINS I.F., MUHUNTHAN B., QU B. (2010) – *Thermomechanical state parameter models for sands.* Géotechnique, 60, n. 8, pp. 611-622.

COSENTINI R.M., FOTI S. (2014) – *Evaluation of porosity and degree of saturation from seismic and electrical data.* Géotechnique, 64, n. 4, pp. 278-286.

COTECCHIA F., CHANDLER R. J. (1998) – *One-dimensional compression of a natural clay: structural changes and mechanical effects.* The geotechnics of hard soils-soft rocks: Proceedings, 2nd International Symposium on Hard Soils – Soft Rocks, pp. 103-114, A. A. Balkema, Rotterdam.

COUSSY O. (2004) - *Poromechanics.* John Wiley & Sons.

DAFALIAS Y.F. (1986) – *An anisotropic critical state soil plasticity model.* Mechanics research communications, 13, n. 6, pp. 341-347.

DAFALIAS Y.F. (2016) – *Must critical state theory be revisited to include fabric effects?* Acta Geotechnica, 11, pp. 479-491

DAFALIAS Y.F., MANZARI M.T., PAPADIMITRIOU A.G. (2006) – *SANICLAY: simple anisotropic clay plasticity model.* International Journal for Numerical and Analytical Methods in Geomechanics, 30, n. 12, pp. 1231-1257.

DAFALIAS Y.F., TAIEBAT M. (2013) – *Anatomy of rotational hardening in clay plasticity.* Géotechnique, 63, n**.**16, pp.1406-1418.

DELAGE P., LEFEBVRE G. (1984) – *Study of the structure of a sensitive Champlain clay and of its evolution during consolidation.* Canadian Geotechnical Journal, 21, n. 1, pp. 21-35.

DE SIMONE A., TAMAGNINI C. ( 2005) – *Stress–dilatancy based modelling of granular materials and extensions to soils with crushable grains.* International Journal for numerical and analytical methods in Geomechanics, *29*, n. 1, pp.73-101.

EINAV I. (2007) – *Breakage mechanics – part I: theory.* Journal of the Mechanics and Physics of Solids**,** 55, n**.** 6, pp. 1274-1297.

FOTI S., LAI C.G., LANCELLOTTA R. (2002) – *Porosity of fluid-saturated porous media from measured seismic wave velocities.* Géotechnique, 52, n. 5, pp. 359-373.

FOTI S., LANCELLOTTA R. (2004) – *Soil porosity from seismic velocities.* Géotechnique, 54, n. 8, pp. 551-554.

FOTI S., LANCELLOTTA R., MARCHETTI D., MONACO P., TOTANI G. (2006) – *Interpretation of SDMT tests in a transversely isotropic medium.* In: Proc. 2nd Intl. Conf.

on the Flat Dilatometer, Wash. DC (pp. 275-280).

Fu P., Dafalias Y.F. (2015) – *Relationship between void- and contact normal-based fabric tensors for 2D idealized granular materials.* International Journal of Solids and Structures, 63, pp. 68-81.

Gao Q.F., Hattab M., Jrad M., Fleureau J.M., Hicher P.Y. (2020) – *Microstructural organization of remoulded clays in relation with dilatancy/contractancy phenomena.* Acta Geotechnica, 15, pp. 223-243.

Gao Q.F., Jrad M., Hattab M., Fleureau J.M., Ameur L.I. (2020) – *Pore morphology, porosity, and pore size distribution in kaolinitic remolded clays under triaxial loading.* International Journal of Geomechanics, 20, n. 6, 04020057.

Gens A. (1982) – *Stress–strain and strength characteristics of a low plasticity clay.* (PhD thesis), Imperial College, London, UK.

Guglielmi S., Cotecchia F., Cafaro F., Gens A. (2022) – *Analysis of the micro to macro response of clays to compression.* Géotechnique, pp. 1-21.

Gurtin M.E., Reddy B.D. (2009) – *Alternative formulations of isotropic hardening for Mises materials, and associated variational inequalities.* Continuum Mechanics and Thermodynamics, 21, pp. 237-250.

Hattab M., Chang C.S. (2015) – *Interaggregate forces and energy potential effect on clay deformation,* Journal of engineering mechanics, 141, n.7, 04015014.

Hattab M., Fleureau J.M. (2010) – *Experimental study of kaolin particle orientation mechanism.* Géotechnique, 60**,** n.5, pp. 323-331.

Hattab M., Hammad T., Fleureau J.M., Hicher P.Y. (2013) – *Behaviour of a sensitive marine sediment: microstructural investigation.* Géotechnique, 63, n**.** 1, pp. 71-84.

Hicher P.Y., Wahyudi H., Tessier D. (2000) – *Microstructural analysis of inherent and induced anisotropy in clay.* Mechanics of Cohesive-frictional Materials: An International Journal on Experiments, Modelling and Computation of Materials and Structures, 5, n**.** 5, pp. 341-371.

Houlsby G.T. (1981) - *Study of plasticity theories and their applicability to soils.* (Doctoral dissertation), University of Cambridge, Cambridge, UK.

Houlsby G.T. (2019) – *Frictional plasticity in a convex analytical setting.* Open Geomechanics, 1, pp. 1-10.

Houlsby G.T., Puzrin A.M. (2006) – *Principles of hyperplasticity: an approach to plasticity theory based on thermodynamic principles.* Springer Verlag, London, UK.

Houlsby G.T., Amorosi A., Rojas E. (2005) – *Elastic moduli of soils dependent on pressure: a hyperelastic formulation.* Géotechnique, 55, n**.** 5, pp. 383-392.

Houlsby G.T., Amorosi A., Rollo F. (2019) – *Nonlinear anisotropic hyperelasticity for granular materials.* Computers and Geotechnics, 115, 103167.

Hueckel T., Tutumluer E. (1994 ) – *Modeling of elastic anisotropy due to one-dimensional plastic consolidation of clays.* Computer and Geotechnics, 16, n. 4, pp. 311-349.

Hjiaj M., de Saxcé G. (2008) – *Variational formulation of the Cam-Clay model.* Proceedings, IUTAM Symposium on Theoretical, Computational and Modelling Aspects of Inelastic Media, pp. 165-174, Springer, Netherlands.

Jaky J. (1944) – *The coefficient of earth pressure at rest.* Journal of the Society of Hungarian Architects and engineers, 78, n. 22, pp. 355–358.

Kanatani K.I. (1984) – S*tereological determination of structural anisotropy.* International Journal of Engineering Science, 22, n. 5, pp. 531-546.

Kavvadas M. (1983) – *A constitutive model for clays based on non-associated anisotropic elasto-plasticity.* Proceedings, International Conference on Constitutive Laws for Engineering Materials-Theory and Application, pp. 10-14.

Kim T., Finno R.J. (2012) – *Anisotropy evolution and irrecoverable deformation in triaxial stress probes.* Journal of Geotechnical and Geoenvironmental Engineering, 138, n**.** 2, pp. 155-165.

Ku T., Mayne P.W. (2013) – *Yield stress history evaluated from paired in-situ shear moduli of different modes.* Engineering Geology, 152, n. 1, pp. 122-132.

Lewin P.I. (1973) – *The influence of stress history on the plastic potential.* Proceedings, Symposium on the Role of Plasticity in Soil Mechanics, Cambridge, England. (No. Conf Paper).

Marigo J.J., Kazymyrenko K. (2019) – *A micromechanical inspired model for the coupled to damage elasto-plastic behavior of geomaterials under compression.* Mechanics & Industry, 20**,** n**.** 1, p. 105.

Martinez-Nistal A., Veniale F., Setti M., Cotecchia F. (1999) – *A scanning electron microscopy image processing method for quantifying fabric orientation of clay geomaterials.* Applied Clay Science**,** 14, n. 4, pp. 235-243.

Maugin G.A., Muschik W. (1994) – *Thermodynamics with internal variables. I. General Concepts, II. Applications.* Journal of Non-Equilibrium Thermodynamics, 19, pp. 217-249, pp. 250-289.

Maugin G.A. (2015) – *The saga of internal variables of state in continuum thermo-mechanics (1893-2013).* Mechanics Research Communications, 69, pp. 79-86.

Mitaritonna G., Amorosi A., Cotecchia F. (2014) – *Experimental investigation of the evolution of elastic stiffness anisotropy in a clayey soil.* Géotechnique, 64, n**.** 6, pp. 463-475.

Mitchell J.K. (1956) – *The fabric of natural clays and its relation to engineering properties.* Proceedings of the Thirty-Fifth Annual Meeting of the Highway Research Board, pp. 693-713, Highway Research Board.

Nguyen Q.S. (2003) – *On shakedown analysis in hardening plasticity.* Journal of the Mechanics and Physics of Solids, 51, n**.**1, pp. 101-125.

Nguyen G.D., Einav I. (2009) – *The energetics of cataclasis based on breakage mechanics.* Pure and applied geophysics, 166, pp. 1693-1724.

OLSEN H.W. (1962) – *Hydraulic flow through saturated clays*. Clays and Clay Minerals, 11, n.1, pp. 131-161.
PAGANO A.G., MAGNANIMO V., WEINHART T., TARANTINO A. (2020) – *Exploring the micromechanics of non-active clays by way of virtual DEMexperiments*. Géotechnique, 70, n. 4, pp.303-316.
PEDROTTI M., TARANTINO A. (2018) – *An experimental investigation into the micromechanics of non-active clays*. Géotechnique, 68, n. 8, pp. 666-683.
PENNINGTON D.S., NASH D.F.T., LINGS M.L. (1997) – *Anisotropy of G0 shear stiffness in Gault Clay*. Géotechnique, 47, n. 3, pp. 391-398.
RICE J.M. (1971) – *Inelastic constitutive relations for solids: an internal variable theory and its applications to metal plasticity*. J. Mech. Phys. Solids, 19, pp. 433-455.
ROLLO F., AMOROSI A. (2020) – *SANICLAY-T: Simple thermodynamic-based anisotropic plasticity model for clays*. Computers and Geotechnics, 127, 103770.
ROLLO F., AMOROSI A. (2022) – *Isotropic and anisotropic elasto-plastic coupling in clays: a thermodynamic approach*. Int. Journal of Solids and Structures, 248, 111668.
RUBIN M.B. (2001) – *Physical reasons for abandoning plastic deformation measures in plasticity and viscoplasticity theory*. Archives of Mechanics, 53, nn. 4-5, pp. 519-539.
SMART P., TOVEY N.K. (1982) – *Electron microscopy of soils and sediments: techniques*. Oxford University Press, Oxford, UK.
SMART P. (1969) – S*oil structure in the electron microscope*. Proceedings, International Conference on Structure, Solid Mechanics Engineering Design Civil Engineering Material. University of Southampton, United Kingdom.
SMITH P.R., JARDINE R.J., HIGHT D.W. (1992) – *The yielding of Bothkennar clay*. Géotechnique, 42, n. 2, pp. 257-274.
TERZAGHI K., PECK R.B. (1948) – *Soil mechanics. Engineering Practice*, John Wiley and Sons, New York.
ULLOA J., ALESSI R., WAMBACQ J., DEGRANDE G., FRANCOIS S. (2021) – *On the variational modeling of non-associative plasticity*. International Journal of Solids and Structures, 217, pp. 272-296.
UYANIK O. (2019) – *Estimation of the porosity of clay soils using seismic P-and S-wave velocities*. Journal of Applied Geophysics, 170, 103832.
WANG R., DAFALIAS Y.F., FU P., ZHANG J.M. (2020) – *Fabric evolution and dilatancy within anisotropic critical state theory guided and validated by DEM*. Int. J. of Solids and Structures, 188, pp. 210-222.
YOON H.K., LEE J.S. (2010) – *Field velocity resistivity probe for estimating stiffness and void ratio*. Soil Dynamics and Earthquake Engineering, 30, n. 12, pp. 1540-1549.
YU C.Y., CHOW J.K., WANG Y.H. (2016) – *Pore-size changes and responses of kaolinite with different structures subject to consolidation and shearing*. Engineering Geology, 202, pp. 122-131.
ZDRAVKOVIC L., JARDINE R.J. (1997) – *Some anisotropic stiffness characteristics of a silt under general stress conditions*. Géotechnique, 47, n. 3, pp. 407-437.
ZHAO C.F., PINZÓN G., WIEBICKE M., ANDÒ E., KRUYT N.P., VIGGIANI G. (2021) – *Evolution of fabric anisotropy of granular soils: X-ray tomography measurements and theoretical modelling*. Computers and Geotechnics, 133, 104046.
ZHENG Y., BAUDET B.A., DELAGE P., PEREIRA J.M., SAMMONDS P. (2022) – *Pore changes in an illitic clay during one-dimensional compression*. Géotechnique, pp. 1-16.
ZIEGLER H. (1977) – *An Introduction to Thermomechanics*. North-Holland, Amsterdam.
ZOUAIN N., PONTES FILHO I., BORGES L., DA COSTA L. M. (2007) – *Plastic collapse in non-associated hardening materials with application to Cam-clay*. International journal of solids and structures, 44, n.13, pp. 4382-4398.
ZOUAIN N., PONTES I., VAUNAT J. (2010) – *Potentials for the modified Cam-Clay model*. European Journal of Mechanics-A/Solids, 29, n. 3, pp. 327-336.

## Una prospettiva microstrutturale alla modellazione costitutiva delle argille

*Le argille sono ampiamente diffuse nelle applicazioni geotecniche e di ingegneria ambientale e la comprensione del loro complesso comportamento meccanico è essenziale per progettare e realizzare strutture sicure ed efficienti. Nel corso degli anni sono stati sviluppati numerosi modelli costitutivi per descrivere il loro comportamento meccanico, ma solo pochi di essi sono stati formulati tenendo conto esplicitamente del complesso comportamento microstrutturale di questi materiali.*

*L'obiettivo di questo articolo è fornire una panoramica di alcuni recenti sviluppi nella modellazione costitutiva delle argille ispirata da una serie di osservazioni microstrutturali. Dopo una disamina delle evidenze sperimentali multi scala e della loro possibile interpretazione e generalizzazione in termini di variabili interne che controllano la meccanica dei terreni argillosi, vengono proposti due esempi di modelli costitutivi, entrambi sviluppati nell'ambito della Termodinamica con Variabili Interne. Questo quadro teorico si dimostra efficace nel consentire lo sviluppo di modelli costitutivi che non solo rispettano i principi fondamentali della termodinamica, ma traggono anche un beneficio diretto dalla comprensione della complessa micromeccanica dei terreni argillosi.*